SiS line emission as a probe of chemistry and grain formation in circumstellar envelopes of AGB stars

Jeanette Bast

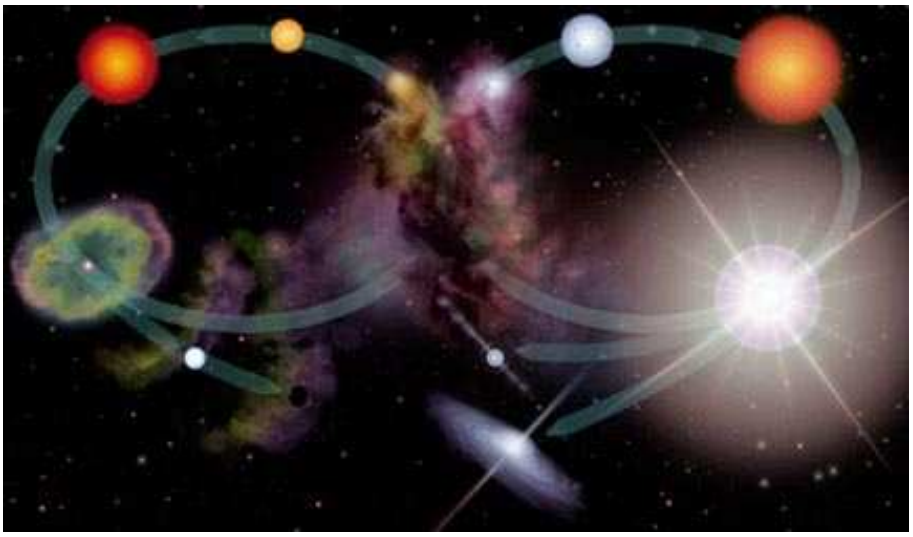

Master's Thesis 20 p

Department of Astronomy
Stockholm University

February 19, 2007

To Thomas, for always being there for me.

Abstract

The stellar interiors of low mass stars are considered to be one of the most important factories in galaxies that are responsible for the formation of more heavy atoms like, e.g., carbon. During the AGB phase nucleosynthesised species get transported to the surface of the star where they will be expelled into the interstellar medium through extensive mass loss from the star. In addition, the CSEs around AGB stars can themselfs have a rich and complex chemistry. The various chemical processes occurring in AGB stars are therefore very important to understand as they relate to the chemical evolution of galaxies. 17 AGB stars have been studied in this diploma thesis project with the help of multi-transition SiS line observations in the radio regime. An extensive and detailed radiative transfer modelling has been performed in order to estimate reliable abundances and look for possible trends with stellar parameters such as the photospheric C/O ratio and mass loss rate. The results clearly show that the SiS abundance is sensitive to the C/O-ratio in the photosphere and that the production of SiS is favoured in carbon stars relative to M-type AGB stars. Also a correlation between the mass loss rate and the fractional SiS abundance have been found for the carbon stars, corroborating earlier research on the related molecule SiO. This indicates that SiS molecules are effectively accreted onto dust grains at higher mass loss rates. The results opens for the possibility that CSEs include processes that can protect newly formed molecules from eventual interstellar photodissociation. This also means that some of the molecules possibly can be redistributed back into the interstellar medium were they will be able to contribute to the enrichment and evolution of more complex molecules in star and planet forming regions.

Contents

Chapter 1

Introduction

Some of the most important questions in astrochemistry is how and where complex molecules form in space, and how they are returned back to the interstellar medium (ISM). The aim of this diploma thesis project is to provide additional information that will help answering these questions. Circumstellar envelopes (CSEs) around AGB (asymptotic giant branch)-stars have been proven to provide a good environment for the formations of a wide variety of molecules. To date 63 different molecular species have been detected in CSE around AGB stars including more complex organic species such as eg., H_2CO. Some of these molecules are unique to the circumstellar medium and have yet not been detected in the ISM. AGB stars will with their strong winds be able to redistribute these molecules back into the ISM. Of interest is therefore to know if these molecules produced in the CSEs can survive and be injected into the interstellar medium. One possibility is for the molecules to be incorporated into the growing dust grains that are formed in the CSEs.

In this project the formation of SiS molecules, in the two different types of chemical environments (M-type stars and carbon stars), will be studied. The study of circumstellar molecules will help constrain chemical models and increase the knowledge about how more complex molecules form in the photospheres and CSEs of AGB stars. Another important aspect of this diploma thesis is to investigate how the SiS abundance varies with stellar parameters such as the C/O-ratio and mass loss rate.

Similar studies have been performed for the SiO molecule by Gonzales Delgado et al. (2003) and Schöier et al. (2006), where the SiO abundance was studied in a sample of both M-type stars and carbon stars. It was discovered that the SiO abundance decreased when the mass loss rate increased which is interpreted as a strong indication that the SiO molecules are condensed onto dust grains, (see Fig. 1.1). This effect could be seen in both types of stars, further supporting such an interpretation. These results are very interesting and indicate that dust plays an important role in the circumstellar chemistry of AGB stars, something that is usually neglected in chemical models. Another important conclusion from these articles is that there appears to be no significant difference between the SiO abundance in M-type stars and carbon stars, which do not agree with equilibrium chemical models, indicating a significant importance of non-equilibrium processes (this can also be seen in fig.1.1). The results in this diploma thesis will be compared with the results from the SiO

observations to see how these two molecules, with rather similar physical and chemical conditions, differ in their formation in CSE around AGB stars and possible redistribution back to the interstellar medium.

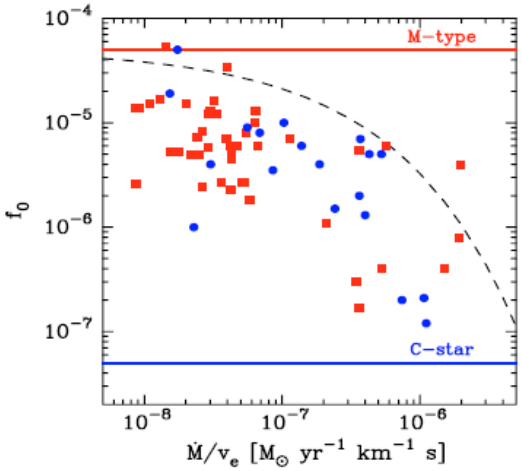

Figure 1.1: The SiO fractional abundance as a function of a density measure ($\dot{M}/v_e$). The red squares are standing for M-type stars and the blue dots for carbon stars. The red and blue solid lines represents the constant abundance of SiS in respectively M-type stars and carbon stars according to chemical models. The dashed line is the expected fractional abundance of SiO for a model with absorption of SiO onto dust grains included in it (adopted from Schöier et al. (2006)).

Chapter 2

Theoretical background

2.1 AGB stars

[1]Up to 90% of all the stars in a galaxy are of low mass and will eventually evolve into AGB stars before they end their lives as planetary nebulae (PN). These stars will have an impact on the evolution of galaxies which make them very interesting objects to study. The evolution from a new born star to a planetary nebula and white dwarf is today rather well defined. However an AGB star's physical processes like chemistry, structure and kinematics is still not so well understood. More observations are therefore needed in order to increase our knowledge more about these stellar objects.

An AGB star is a red giant star on the asymptotic giant branch (AGB). It is very luminous ($\sim$6000 $L_{\odot}$), has a strong stellar wind ($\sim$10-20 km/s) which leads to a high mass loss rate ($\sim 10^{-8}$-10^{-5} $M_{\odot}$ yr^{-1}. These stars have an effective temperature of around 2500 K and a very large radius of about $\sim$ 2 AU ($\sim 3.0 \cdot 10^{13}$ cm). They are pulsating objects with well defined periods of about 50-500 days.

In this project two types of AGB-stars are studied, M-type AGB stars and carbon stars. The M-type AGB stars will throughout this diploma thesis report be called just M-type stars. The major difference between these two types is that the C/O ratio in their photosphere is larger than unity in carbon stars and lower than unity in M-type stars. The difference in the C/O ratio in the photosphere is leading to differences in the formation of molecules so that certain types of molecules are favoured in one or the other of the two star types.

2.1.1 The evolution from new born star via AGB star to white dwarf

Interstellar clouds that are massive enough will eventually contract and form a star. When the stellar core is warm enough nuclear reactions will start, where hydrogen will form helium through fusion. The star will then move to the main sequence (MS) where it will spend most of its life. The Sun is now on the MS

[1]Information is taken from: the thesis Winds from red giant stars, F. Schöier, 2000; Stellar structure and evolution, J. Christensen-Dalsgaard, 2003; Asymptotic giants branch stars, H. Olofsson and H. Habing, 2003.

and has been there for about 4.5 Gyr and will continue to be so during the next 6.4 Gyr.

Compared to their later evolutionary stages the MS is the most stable episode in their lives. They will continue being at the MS until they have burned all their hydrogen in their core. When the hydrogen burning ceases in the core it will start to contract, even though hydrogen burning continues in a shell around the stellar core. This leads to an expansion of the outer layers which will increase both the luminosity and the radius of the star. The stellar surface temperature will however decrease, which will make it appear red. As a consequence of these effects these stars are now called red giant stars. The Sun will according to models (Sackmann et al. 1993) have a radius about the size of Venus' orbit and a luminosity of around 2350 $L_{\odot}$ when it is in its red giant phase.

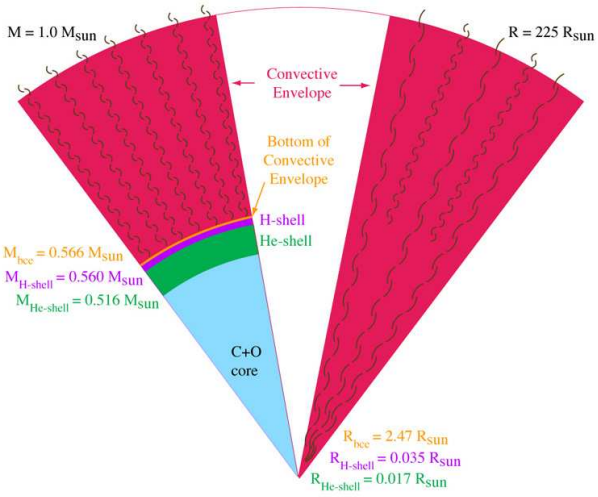

Figure 2.1: An illustration of the inner structure of an AGB star, (http://www.cococubed.com/images/agb/).

The core will continue to contract until helium starts to burn. The helium burning phase will start by a run away process if the stellar mass is below 1 $M_{\odot}$, because of its electron degenerated core. This is a consequence that can be explained by the cores inability to expand when the temperature of the core rapidly increases during the ignition of helium. The run away results in a helium flash that will remove the degeneracy in the core and make the star expand again. Stars with higher masses do not have degenerated cores so their outer layers will just expand when hydrogen burning begins. An illustration of the morphology of an AGB star is shown in Fig. 2.1.

The star is said to move to the horizontal branch (HB) when the helium burning has started, see Fig. 2.2. This period is also rather stable even though it do not last long. For the Sun will the HB phase be about 0.1 Gyr long, about 1 % of its total life time. The core will start to collapse when all the helium has been consumed which will once again lead to an expansion of the outer layers of the star and it will again transform into a red giant star. The helium will continue to burn in a shell between the core and hydrogen burning shell. The star has now entered the AGB and is therefore called an AGB star. The

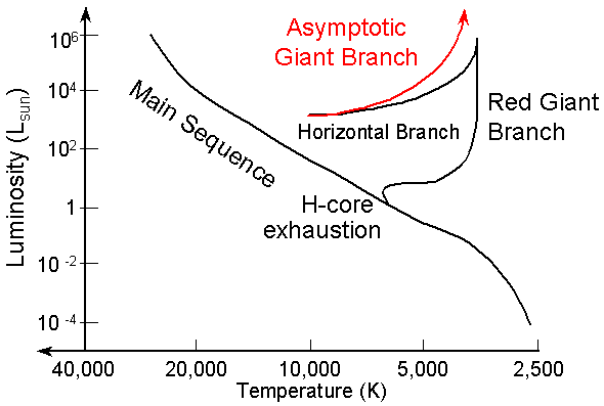

Figure 2.2: The evolution of a low mass star plotted in the "Color-Magnitude" diagram, (http://www-astronomy.mps.ohio-state.edu/ pogge/Ast162/Unit2/Images/hragb.gif).

combination of a hydrogen and helium burning shell with a C/O core leads to a very unstable environment. The instabilities results in a pulsating star with high mass loss rates and dredge ups, where oxygen and carbon is transported to the surface of the star. The star will remain on the AGB until it has lost nearly all material by its strong stellar wind until just the hot stellar core of the star will be left. The rapid increase of temperature and radiation when all the matter has left the core will ionize the surrounding CSE so that a PN will form (see Fig. 2.3). In the middle of the PN a white dwarf can be found, which is just the stellar core that is beginning to lower its temperature by radiating away heat. A summary of the evolution of a low mass star can be seen in Fig. 2.2.

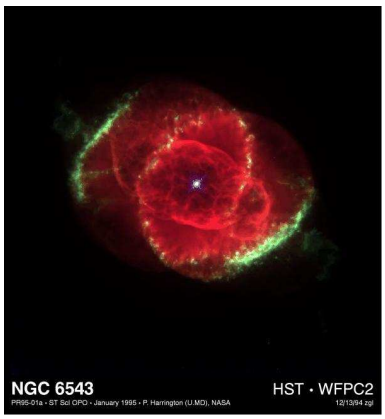

Figure 2.3: The Cat's Eye Planetary Nebula (NGC 6543), (http://courses.nnu.edu/ph106wj/images/Ngc6543.jpg).

2.1.2 Circumstellar envelopes and dust grain formation

The pulsations of AGB stars induce shockwaves in their atmospheres and CSEs. These shockwaves will benefit the formation of dust grains that have the ability to absorb higher frequency photons and remit them at longer wavelengths. The dust grains will during this process gain some of the absorbed photons momentum so that they will start to accelerate outwards. The dust grains are coupled to the gas through collisions which leads to an outward motion for the gas as well. This results in a high mass loss from the star that will distribute the gas and dust grains out from the star, forming a CSE around the star that eventually will merge into the interstellar medium. This process is illustrated in Fig. 2.4.

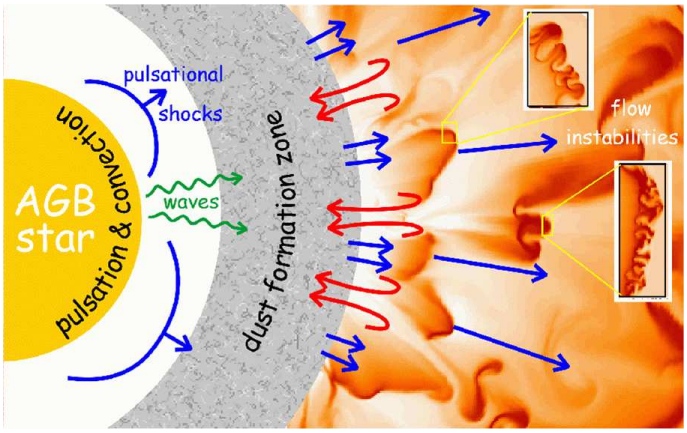

Figure 2.4: The dust formation in CSE around AGB stars, (http://www.strw.leidenuniv.nl/~woitke/).

The shocks in the cool atmospheres of AGB stars are creating an advantageous environment for formation of various amount of molecular species. The ratios between the different kinds of molecules are sensitive of the C/O-ratio. The best way today to learn about the photospheric chemistry in high mass loss rate AGB stars through observations is to observe the radiation from CSE around the AGB star and extrapolate the results backwards. The reason for this is that the emission from the atmosphere in most cases can not be directly observed, because of thickness of the gas and dust around the star.

2.2 Radiation transport

[2]It is very important to understand the theory of radiative transport to learn more about how to interpretate spectral line observations in order to extract local physical and chemical properties of the gas. In this section some of the basic equations in radiative transport will be reviewed. Concepts like LTE (local thermodynamic equilibrium), brightness temperature, excitation temperature and statistical equilibrium will also be explained.

[2]The equations in this section is taken from Interpreting astronomical spectra, D.Emerson, 1997 and from the thesis: Winds from red giant stars, F.L. Schöier, 2000.

2.2.1 The radiative transfer equation, brightness and excitation temperature

The energy flow, per unit area, per unit time, per solid angle from a source is described by the intensity (I). The intensity is distance independent and would therefore be the same value wherever it is measured if there would not be any material in between that could affect the intensity. In reality there is always something that will affect the intensity by absorption or emission of the radiation. This interaction between the radiation and the material makes it possible to determine local properties of the material such as density, velocities, temperatures, dust composition, molecular abundances etc.

The emission coefficient j_ν and absorption coefficient α_ν are used to describe the change in the intensity,

$$dI_\nu = -I_\nu \alpha_\nu dx + j_\nu dx \tag{2.1}$$

where $-I_\nu \alpha_\nu dx$ is how much of the intensity that will be absorbed and j_ν is how much intensity that will be contributing to the total intensity after a physical step dx through the medium . A usual way to express the same equation is:

$$\frac{dI_\nu}{d\tau_\nu} = I_\nu - S_\nu \tag{2.2}$$

where $d\tau_\nu = \alpha_\nu dx$ is the optical depth and $S_\nu = j_\nu/\alpha_\nu$ is the source function.

Notice also that the signs have been changed so that the intensity I is positive outwards to the observer and so that $d\tau_\nu$ and dx is starting at zero closest to the observer. Equation 2.2 is the basic equation of radiative transfer. This equation can be solved and written in its integrated form equation 2.5 through the following steps:

$$\frac{d}{d\tau}(Ie^{-\tau}) = Se^{-\tau} \tag{2.3}$$

$$I(\tau_0)e^{-\tau_0} - I(\tau_b)e^{-\tau_b} = \int_{\tau_0}^{\tau_b} S(\tau)e^{-\tau}d\tau \tag{2.4}$$

$$I(\tau_0) = I(\tau_b)e^{-(\tau_b-\tau_0)} + \int_{\tau_0}^{\tau_b} S(\tau)e^{-(\tau-\tau_0)}d\tau \tag{2.5}$$

where $I(\tau_0)$ is the intensity that is leaving the medium and measured by the observer and $I(\tau_b)$ is the intensity that is entering the medium.

It is unfortunately not as easy to estimate the intensities as is looks. The reason for the complexity is that the optical depth τ is dependent on the absorption coefficient α, which depends on the excitation of the molecule that is dependent on I_ν and so on. This means that iterations are generally needed to solve the above equations. As we shall see in section 2.2.2 the local mean intensity $\bar{J}$ is an important quantity in the models to calculate the level populations n_i. The mean intensity $\bar{J}$ is calculated by equation,

$$\bar{J_\nu} = \frac{1}{4\pi}\int I_\nu d\Omega \tag{2.6}$$

where $d\Omega$ is the change in the solid angle Ω.

The intensity for a blackbody is described by Planck's law:

$$I_\nu = \frac{2h\nu^3}{c^2}\frac{1}{e^{h\nu/kT}-1} \tag{2.7}$$

where, c is the speed of light, h the Planck's constant, ν the frequency, k the Boltzmann constant and T the temperature.

In radio and mm observations is it customary to give the intensity in brightness temperature, ie., the temperature that the source is needed to have to give the radiation that represents the blackbody temperature. The brightness temperature T_b is derived from Plank's law where the Rayleigh-Jeans approximation is used.

Rayleigh-Jeans approximation (applicable when $h\nu/kT \ll 1$):

$$I_\nu = \frac{2h\nu^3}{c^2}\frac{1}{e^{h\nu/kT}-1} \approx \frac{2\nu^2 kT}{c^2} \tag{2.8}$$

where the Taylor expansion:

$$e^x = 1 + x + ... \tag{2.9}$$

can be used when $x \ll 1$.

This will give the brightness temperature:

$$T_b = \frac{I_\nu c^2}{2k\nu^2} \tag{2.10}$$

which can be used irrespective if the source is a blackbody or not; it is just a way of expressing the intensity. In a similar way the source function S_ν can be expressed by the excitation temperature T_ex, the temperature a blackbody would need to have to give the actual source function. In the Rayleigh-Jeans limit this can be described by:

$$S_\nu = \frac{2kT_{ex}}{c^2}\nu^2 \tag{2.11}$$

2.2.2 Local thermodynamic equilibrium (LTE) and non-LTE

In thermodynamic equilibrium (TE) many of the physical quantities can be related to the equations of statistical mechanics. This for example means that the Boltzmann equation will describe the excitation, the Saha equation will give the ionization and the source function can be set to be equal to the Planck function.

The stellar atmospheres can not be described by TE because this would require the atmospheres to have the same temperature everywhere and no net flow of radiation. The usual way is instead to use the approximation local thermodynamic equilibrium (LTE), where TE is assumed in smaller restricted parts of

the atmosphere. Each part is set to have the same temperature everywhere and that the radiation is isotropic in it. This is however just applicable to regions with higher densities and at larger optical depths. (A good way, even though not easy, in astronomy to check if LTE is a good approximation or not is to calculate the excitations temperature and see if it is the same as the kinetic temperature or not. LTE is a good approximation if the both temperatures are close to the same value. It can be seen in Fig. 4.2 in section 4.4 that this is generally not the case for most of the AGB stars. This means that their level populations n_i of SiS can not be calculated from the Boltzmann equation.The statistical equilibrium equations (SE) are instead used to derive n_i. This is called to use a non-LTE model.

In statistical equilibrium the absorption and emission coefficients are described by,

$$j_{ij}(\nu) = n_i A_{ij} \phi_{ij}(\nu) \tag{2.12}$$

$$\alpha_{ij} = (n_j B_{ji} - n_i B_{ij} \phi_{ij}(\nu) \tag{2.13}$$

for a multilevel molecule, with i representing the upper levels and j the lower levels in a transition $j \rightarrow i$. A_{ij} is the Einstein probability for spontaneous emission, B_{ij} for stimulated emission and B_{ji} for absorption. The population densities of the upper level are given by n_i and the lower by n_j. The line profiles for the transitions are here set to be the same for all transitions.

Equation 2.12 and 2.13 can in turn be used to derive the source function in SE.

$$S_\nu = \frac{j_{ij}}{\alpha_{ij}} = \frac{n_i A_{ij}}{n_j B_{ji} - n_i B_{ij}} \tag{2.14}$$

The level populations n_i and n_j can be derived from solving the statistical equilibrium equation.

$$\sum_{j<l} [n_j A_{jl} + (n_j B_{jl} - n_l B_{lj}) \bar{J}_{jl}] - \sum_{j<l} [n_l A_{lj} + (n_l B_{lj} - n_j B_{jl}) \bar{J}_{lj}] + \sum_j [n_j C_{jl} - n_l C_{lj}] = 0 \tag{2.15}$$

where C_{jl} and C_{lj} are the collisional rate coefficients.

2.3 Radio telescopes

[3]This thesis is based on observations made by three different radio telescopes: JCMT (James Clerk Maxwell's telescope), OSO (Onsala Space Observatory) 20 m telescope and APEX (Atacama Pathfinder Experiment). A brief and general explanation how these types of radio telescopes are constructed and how they are functioning will be given here. Some of the terminology often used in radio astronomy will also be introduced in this section.

A radio telescope can be constructed in several different ways depending on which wavelength region it is intended for. The radio telescopes that have been used during our observations are all constructed in a similar way. They

[3]Equations in this section are taken from: Astrophysical techniques, Kitchin, 2003

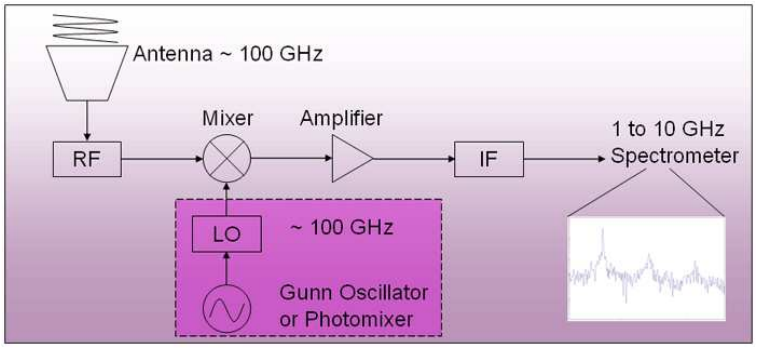

Figure 2.5: A schematic picture of a heterodyne receiver, (http://www.sr.bham.ac.uk/yr4pasr/project/photomixers/images/Heterodyne-Receiver.gif).

all have an antenna that consists of a sensor and a disc, and a receiver that will detect and amplify the signal. The sensor is a SiS (super conductor-insulator-superconductor) device detector. It consists of two layers of a superconducting film. When a photon hits the detector an electron will absorb it and tunnel trough the insulator barrier between the films into the other superconducting film which will transport it further to the receiver. The receiver in these cases are a heterodyne receiver, see Fig. 2.5. The receiver transports the electric signal from the SiS detector through several amplifiers to another detector. That detector will then send out a new signal that will be integrated for a while so that the noise level can be reduced before it is transported to the output device that is connected to a computer.

There are many similarities between an optical telescope and a radio telescope. One of these is that their sensitivity to electromagnetic radiation can be described in similar ways. However, tradition has formed two different types of sensitivity diagrams. The optical telescopes power is usually described by diffraction diagrams whereas radio astronomers usually use a polar diagram. A polar diagram of a half-wave dipole can be seen in Fig. 2.6(a). This two dimensional figure is just a cross section of the beam pattern which is more correctly described by a three dimensional diagram where the beam pattern is building up a torso around the dipole's long axis, see Fig.2.6(b)

Several half-wave dipoles are usually connected in an array which will make the antenna more sensitive in the direction of its optical axis. The antennas gain in the main lobe can be improved even more if a reflector is placed behind the dipole. A reflector and other elements that will improve the gain of the antenna and that are not part of the antennas electric circuit are called parasitic elements. There are four different terms that are usually describing an antennas capability to receive electromagnetic radiation: BW(HP) = beam width at half power, BW(FN) = beam width at first nulls, the gain and the effective area.

BW(HP) = The angular distance between the two points where the output power of the antenna has fallen to half of its maximum value.

BW(FN) = The angular distance between the first two points, one on each side

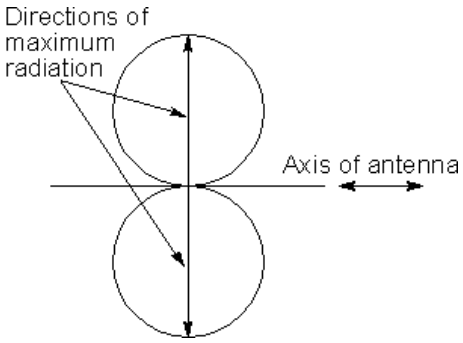

(a) Polar diagram of a half-wave dipole.

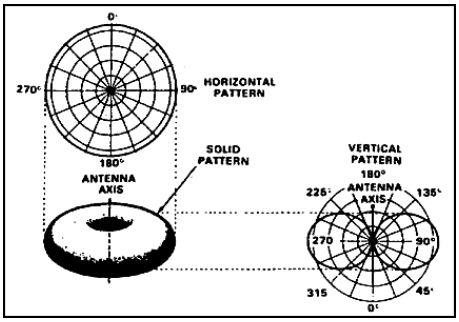

(b) Three dimensional polar diagram of a half-wave dipole.

Figure 2.6: Polar diagrams of a half-wave dipole illustrated in 2 and 3 dimensions, (http://www.radio-electronics.com/info/antennas/dipole/dipolepolardiag.gif and http://www.radiowavz.com/ANTENN 1/img049.gif).

of the optical axes, where the antennas sensitivity has fallen to zero. BW(FN) is 180^o in a half-wave dipole, se Fig. 2.6.

$$BW(FN) = 2 \cdot \frac{1.22\lambda}{D} \tag{2.16}$$

Gain = Maximum output power / Average output power

Effective area A_e:

$$A_e = \frac{P_\nu}{F_\nu} \tag{2.17}$$

where P_ν is the power output by the antenna at frequency ν and F_ν is the correctly polarized flux from the source at the antenna frequency ν.

The gain g and the effective area A_e are related trough equation:

$$g = \frac{4\pi}{c^2}\nu^2 A_e \tag{2.18}$$

The telescopes resolution is given by the Rayleigh resolution α, which is the smallest angular distance that two point sources can have in between them and still be resolved by a telescope with diameter D.

$$\alpha = \frac{1.22\lambda}{D} = \frac{BW(FN)}{2} \tag{2.19}$$

This means that big discs are required if you want a good resolution during radio wave observations. Big discs are always much more difficult to build but the Rayleigh limit $\lambda/20$ is also allowing the deviations from a parabolic surface to be bigger which is making the building process easier. The Rayleigh limit is giving the largest deviations a disc can have from a paraboloid surface before it starts to worsen the telescopes resolution. A smaller limit: $\lambda/20$ is usually used to be on the safe side.

2.3.1 The main beam efficiency and antenna temperature

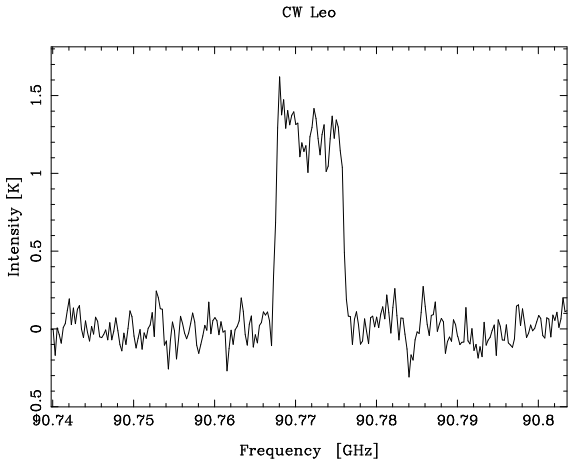

Figure 2.7: Example of an observed spectrum with the intensity given in T_A^* scale. This is the J=5-4 rotational transition of SiS taken with the OSO 20 m telescope.

[4]The sensitivity or gain of the heterodyne receiver is given in the antenna temperature T_A^*, which is measured in Kelvin. This is therefore the unit on the y-axis in the observed spectra, see Fig. 2.7. T_A^* is the temperature that is giving the intensity that we would measure outside of the earth atmosphere. The observed spectra that is sent to the observers from the telescope is in the T_A^* scale, because it is already at the telescope corrected for the atmospheric effect on the data. The reduction process that is left to do for the observer is then consisting of subtracting a baseline from the spectrum and divide the antenna temperature with the main beam efficiency to correct the beam patterns side

[4]Equations in this section are taken from: Guide to spectral line observing at JCMT, http://docs.jach.hawaii.edu/JCMT/HET/GUIDE/

wings for its non Gaussian form, see section 3.5.2. All the reduced spectra in appendix A are in main beam brightness temperature (T_{mb}) scale, which is given by:

$$T_{mb} = \frac{T_A^*}{\eta_{mb}} \tag{2.20}$$

where η_{mb} is the main beam efficiency.
A description how to calculate the main beam efficiency is given here:

Main beam efficiency

The main beam efficiency is calculated with the help of equation 2.21

$$\eta_{mb} = \frac{T_A^*}{T_A^{*'}} \tag{2.21}$$

where $T_A^{*'}$ is the predicted antenna temperature for a planet with a known continuum strength and T_A^* is the measured antenna temperature of the planet.

$$T_A^{*'} = T_b \eta_{gauss} \tag{2.22}$$

where T_b is the planets brightness temperature and where

$$\eta_{gauss} = 1 - 2^{D/BW^2} \tag{2.23}$$

BW is the beam width and D the diameter of the planet.

The main beam efficiency is regularly measured at the telescope and provided to the astronomer.

Chapter 3

Observations and reduction

The observations which this diploma thesis is based on were performed with the three radio telescopes: JCMT, APEX and OSO 20 m telescope. Some basic knowledge about the observing runs and some characteristics of the telescopes will be given in this section. A more detailed description of the observational techniques at the APEX telescope will also be given. The initial part of the diploma thesis work consisted of sending in a proposal to obtain high frequency SiS observations for a large number of AGB stars using the APEX telescope. The proposal (see Appendix B) was accepted and observations were made in service mode between 1-3 of July, 2006. The APEX observations form an important part of the large data set that this diploma thesis is based on.

The diameters of the telescopes are 12 m (APEX), 15 m (JCMT) and 20 m (OSO). All three telescopes have SIS receivers, which is the most commonly used type of receiver today at radio telescopes. Some of the characteristics of the telescopes can be found in table 3.1.

Telescope	Receiver	Spectrometer	Observed lines	Bandwidth	Spectral resolution
APEX:	APEX-2A	FFTS	20 → 19:	0.42 GHz	1.211 MHz
			19 → 18:	0.29 GHz	1.151 MHz
JCMT:	B3	DAS	19 → 18	1.8 GHz	1.250 MHz
	A3:		12 → 11	950 MHz	625 kHz
	B3		19 → 18	1.8 GHz	1.250 MHz
OSO:	100 GHz receiver	Mul A:	6 → 5	512 MHz	1 MHz
			5 → 4	512 MHz	1 MHz
		Mul B:	6 → 5	64 MHz	250 kHz
			5 → 4	64 MHz	250 kHz
		LRCOR	6 → 5	640 MHz	400 kHz
			5 → 4	640 MHz	400 kHz

Table 3.1: Telescope information. The bandwidths and spectral resolutions are taken from the data.

3.1 The APEX telescope

The APEX (Atacama Pathfinder Experiment) telescope is a submillimeter telescope positioned on the high altitude site of Llano Chajnantor in the Atacama desert in Chile, on an altitude of 5104 m. It has been operating since July

2005 and it is constructed to be an ALMA (Atacama Large Millimeter Array) prototype antenna. The planning and construction of the telescope is done in a collaboration between Max Planck Institute für Radioastronomie (MPifR) 50 %, Onsala Space Observatory (OSO) 23 % and the European Southern Observatory (ESO) 27 %. The telescope can be seen in Fig. 3.1.

Figure 3.1: The APEX telescope at the Llano Chajnantor site, (http://www.universetoday.com/am/uploads/ut_sat.jpg).

3.2 Observing at the APEX telescope

The observation usually starts by doing pointing and focusing checks. This is typically done by observations of circumstellar envelopes of late-type stars with strong spectral lines. In the case of APEX's receiver APEX-2A, usually the CO rotational transition J = 3-2 is recommended. The same line is also used for the JCMT telescope which also can use the CO rotational transition J = 2-1 and depending on the receiver being used strong continuum sources. The pointing and focusing checks are usually done by observations of strong SiO masers for the OSO telescope. A calibration of the telescope is also needed and this is done using the chopper wheel method. This means that the sky is observed and two loads with known temperatures. It is also important to take a standard spectrum at the beginning of each observing run.

The observing technique that is currently available at the APEX telescope is position switching. The telescope is then physically moving between observing the object of interest and a reference position that do not emit any strong emission lines within the observed frequency interval. In our observations the reference position was chosen to be located +3' in azimuth from the star.

Another technique that is used at OSO and JCMT is the beam switching technique. This technique is used in all observations taken with both the JCMT and OSO telescopes. The major difference between these methods is that instead of moving the entire telescope only the secondary mirror is adjusted so that the light from the object is varying between the two beams in the beam switching technique. This technique is flattening the baselines more, because of its time saving ability. It goes faster to change the inclination of the secondary mirror than moving the entire telescope. The time reduction between observing

Source	D [pc]	$L_\star$ [$L_\odot$]	$T_\star$ [K]	$\dot{M}$ [$M_\odot$ yr^{-1}]	v_e [km s^{-1}]	τ_{10}	r_i [cm]	r_e [cm]
M-stars:								
GX Mon	540	8000	1800	$2.0\cdot10^{-5}$	18.0	0.40	$2.0\cdot10^{14}$	$2.2\cdot10^{16}$
IK Tau	250	6900	2800	$1.0\cdot10^{-5}$	18.0	1.30	$1.2\cdot10^{14}$	$1.6\cdot10^{16}$
IRC-10529	270	10400	1800	$2.5\cdot10^{-6}$	11.0	3.00	$2.5\cdot10^{14}$	$1.0\cdot10^{16}$
IRC+40004	410	11500	1800	$6.0\cdot10^{-6}$	17.5	0.30	$3.6\cdot10^{14}$	$1.3\cdot10^{16}$
IRC+50137	410	9600	1800	$1.0\cdot10^{-5}$	16.5	2.40	$5.4\cdot10^{14}$	$1.6\cdot10^{16}$
R Cas	220	6000	1800	$1.1\cdot10^{-6}$	8.0	0.20	$1.5\cdot10^{14}$	$0.8\cdot10^{16}$
TX Cam	380	8400	2400	$7.0\cdot10^{-6}$	18.0	0.50	$2.1\cdot10^{14}$	$1.3\cdot10^{16}$
WX Psc	600	7900	2200	$1.0\cdot10^{-5}$	19.0	3.00	$2.2\cdot10^{14}$	$1.5\cdot10^{16}$
C-stars								
CW Leo	120	9600	2000	$1.5\cdot10^{-5}$	14.0	0.90	$1.7\cdot10^{14}$	$2.2\cdot10^{16}$
LP And	630	9400	2000	$1.5\cdot10^{-5}$	13.5	0.60	$1.5\cdot10^{14}$	$2.2\cdot10^{16}$
RV Aqr	670	6800	2200	$2.8\cdot10^{-6}$	15.0	0.27	$7.6\cdot10^{13}$	$9.3\cdot10^{15}$
RW LMi	440	9700	2000	$6.0\cdot10^{-6}$	16.5	0.50	$2.1\cdot10^{14}$	$1.3\cdot10^{16}$
V Cyg	310	6300	1900	$9.0\cdot10^{-7}$	10.5	0.08	$8.7\cdot10^{13}$	$6.4\cdot10^{15}$
V384 Per	560	8100	2000	$3.5\cdot10^{-6}$	14.5	0.25	$1.0\cdot10^{14}$	$1.1\cdot10^{16}$
V821 Her	600	7900	2200	$1.8\cdot10^{-6}$	13.0	0.45	$8.1\cdot10^{13}$	$8.1\cdot10^{15}$
15082-4808	640	9000	2200	$1.0\cdot10^{-5}$	19.0	0.80	$1.9\cdot10^{14}$	$1.5\cdot10^{16}$
15194-5115	500	8800	2400	$9.0\cdot10^{-6}$	21.0	0.55	$1.5\cdot10^{14}$	$1.4\cdot10^{16}$

Table 3.2: Source parameters

the reference position and the object gives an improvement of estimating the atmospheric effect on the data which in turn will flatten the baselines. The beam separation for the OSO and JCMT telescopes where 11' and 2' respectively.

3.3 The sample

The aim of this diploma thesis project is to study the chemistry of SiS through accurate determination of its circumstellar abundance in a large sample of AGB-stars with varying C/O-ratios. The emission from the SiS molecules is usually weaker compared to other molecules such as CO, HCN and SiO, which naturally leads to a bias toward high mass loss rate objects. Stars with lower mass loss rates generally have too weak SiS line emission to be detectable with the telescopes in use here within a reasonable observing time. This is so because the higher mass loss rates is leading to higher densities of molecules in the CSE:s which in turn will lead to stronger SiS line emission.

The sample contains a selected group of 34 M-type stars and carbon stars with low ($\sim10^{-7}$ $M_\odot$ yr^{-1}), intermediate ($\sim10^{-6}$ $M_\odot$ yr^{-1}) and high ($\sim10^{-5}$ $M_\odot$ yr^{-1}) mass loss rates. SiS line emission were however only detected in the intermediate to high mass loss rate stars, in total 17 stars. SiO has earlier been detected by Gonzales Delgado et al. (2003) and Schöier et al. (2006) in the same sample of stars and their results will later be compared with the results derived for SiS in this diploma thesis. These articles are also providing most of the stellar and circumstellar parameters that are used as an input to the model. The sample of the 17 stars and their parameters are given in table 3.2.

The M-type stars are classified as M-type stars in Kholopov et al. (1985). They are all Mira variables, which means that their luminosities are regularly varying from one maximum to another in a period of about 300-800 days. The carbon stars are all classified, and studied in more detail, in Lambert et al.

(1986). They are consisting of 7 Mira variables, one semi regular variable (RW LMi) and one that is approximated to be a semi regular variable (V821 Her) in the calculations of its parameters.

3.4 Observational results

The observations where carried out during 1997-1998 and March 2005 using the OSO 20 m telescope, July 2006 using APEX and 2000 using the JCMT. In total 34 stars were observed and SiS line emission was detected in 17 of them, in 8 M-type stars and 9 carbon stars. A literature search was also performed to find complementary SiS observations. Data from Woods et al. (2003), Bujarrabal et al. (1994) and Olofsson et al. (1998) have been included in the analysis. The integrated intensities of both the observed lines and line intensities from the literature can be found in table 3.3. The integrated intensities are given in T_{mb} scale which means that they have been corrected for the main beam efficiency. The absolute calibration of the line intensities is estimated to be about $\pm$ 20%. The observed rotational transitions of SiS are J=20-19, 19-18, 12-11, 6-5 and 5-4, all in their ground vibrational state ($\nu = 0$).

3.5 Reduction of the data

One important part in this diploma thesis project was to reduce the large set of data from the three different telescopes. The major part of the reduction was done by the use of the xs package that was developed by P. Bergman at Onsala Space Observatory[1]. The procedure of reducing the data and estimating the intensity in the molecular lines can be summarized as followed:

- Detect the molecular emission lines.
- Subtraction of baseline.
- Convert the data from T_A^* to T_{mb}.
- Estimate the integrated intensity in each molecular line.

This procedure will be described in more detail in the following sections.

3.5.1 Identification of the molecular emission lines

It is useful to first reduce the resolution in the spectra, especially if they have high noise levels, before detecting the molecular lines in them. This can be seen in figure 3.2, where the star WX Psc:s spectrum of the SiS rotational line J = 5-4 is shown. The SiS emission line is rather difficult to notice in figure 3.2(a) but when the resolution is reduced in figure 3.2(b) it is much more easy to detect it and to work with when estimating its integrated intensity. 1-4 rotational transition lines from SiS were detected in 17 of 34 observed stars. Each star's detected lines are presented in table 3.3.

Some lines are so weak so that they are difficult to detect. It can therefore be wise to use a method that can determine if it is a real line or just noise. One

[1] ftp://yggdrasil.oso.chalmers.se/pub/xs.

Source	IRAS	Cat.[a]	Tel.[b]	I_{mb} [K km s^{-1}]				
				$5 \rightarrow 4$	$6 \rightarrow 5$	$12 \rightarrow 11$	$19 \rightarrow 18$	$20 \rightarrow 19$
M-stars:								
GX Mon	06500 + 0829	O	OSO	0.2	0.2			
		O	JCMT			1.4		
IK Tau	03507 + 1115	O	OSO		0.4			
		O	JCMT			4.7	9.2	
		A	IRAM	1.2				
		A	OSOH	0.3				
IRC-10529	20077 - 0625	O	OSO		<			
		O	JCMT			1.3		
		O	APEX				1.0	
		A	IRAM	1.1				
IRC+40004	00042 + 4248	O	OSO	<				
		O	JCMT			1.1		
IRC+50137	05073 + 5248	O	OSO	<	0.5			
		O	JCMT			1.5		
R Cas	23558 + 5106	O	OSO	<				
		O	JCMT			<	0.7	
		A	OSOH	< 0.4				
TX Cam	04566 + 5606	O	OSO		0.6			
		O	JCMT			1.5		
		A	IRAM	1.8				
		A	OSOH	0.6				
WX Psc	0137 + 1219	O	OSO	0.4	1.0			
		O	JCMT			4.0		
		O	APEX				4.2	
		A	OSOH	1.4				
C-stars								
CW Leo	09452 + 1330	O	OSO	59.3/56.7				
		O	APEX					158.8
		A	OSOW	39.5	52.4			
		A	SESTW	35.5	30.0			
		A	IRAM	115				
		A	OSOH	40.6				
LP And	23320 + 4316	O	OSO	/2.2				
		A	OSOW	4.1	1.9			
		A	IRAM	4.2				
RV Aqr	21032 - 0024	O	APEX				0.5	
		O	SEST	<				
		A	SESTH	< 0.4				
RW LMi	10131 + 3049	O	OSO	1.0/<				
		A	OSOW	0.6	3.6			
		A	IRAM	3.3				
		A	OSOH	1.3				
V Cyg	20396 + 4757	O	OSO	0.3/				
		A	IRAM	0.8				
		A	OSOH	0.3				
V384 Per	03229 + 4721	O	OSO	0.4/				
		A	OSOH	0.4				
V821 Her	18397 + 1738	O	APEX					1.8
15082 - 4808	15082 - 4808	O	APEX				3.8	
		A	SESTW	1.6	1.1			
		A	SESTH	1.1				
15194 - 5115	15194 - 5115	O	APEX					3.4
		A	SESTW	2.8	2.4			
		A	SESTH	2.4				

[a]O=observed, A=article

[b]OSO, JCMT, SEST and APEX are data taken from recent observations. OSOW=OSO data taken from P.Woods et al. 2003, SESTW=SEST data taken from P.Woods et al. 2003, IRAM=IRAM data taken from V. Bujarrabal et al. 1994, OSOH= OSO data taken from H.Olofsson et al. 1998 and SESTH=SEST data taken from H.Olofsson et al. 1998.

Table 3.3: Observational results.

of these methods is to look at the width of the line which should be around twice the expansion velocity of the circumstellar envelope if it is a real line.

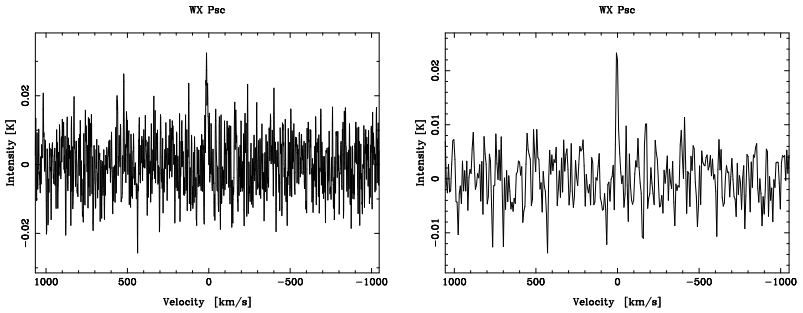

(a) The spectrum with a resolution of 1.3 km/s.

(b) The spectrum with a resolution of 6.6 km/s.

Figure 3.2: The star WX Psc:s SiS rotational transition line J = 5-4. It is observed by the OSO 20 m telescope.

3.5.2 Subtraction of baseline and converting the data from T_A^* to T_{mb}

Each raw spectrum's line free regions is fitted to a low order polynomial line, the baseline. This baseline was then subtracted from the spectrum. The last thing that had to be done before calculating the intensities of the lines is to convert the T_A^* to T_{mb} scale. This is done by dividing the spectrum with the main beam efficiency η_{mb}.

The main beam efficiency is specific for each receiver at a telescope and it is also wavelength dependent. The different main beam efficiencies can be found at the homepages of the telescopes but some of them were needed to be recalculated for the frequencies of interest in this project. This is done by taking the already given values for η_{mb} to some known frequencies and do a first order linear fit. The coefficients from the best linear fit can then be used to calculate better estimates of the η_{mb} for the frequency that is representing the SiS emission line of interest. The main beam efficiencies can be found in table 3.4.

All the reduced spectra can be found in Appendix A. The x-axis is set to be in the relative velocity and each observed lines frequency is set to be the rest frequency which means that the lines will be centered on the rest velocity = 0. Some of the lines might have a small offset from the rest frequency depending of uncertainties in the v_{lsr} (the radial velocity relative to the Solar local standard of rest).

3.5.3 Estimating the integrated intensity in each molecular line

The total intensity of the line can be estimated from integration over the velocity of the reduced line. This is easily done with the help of the xs package. The

Transition	Frequency [GHz]	Telescope	η_{mb}	θ_{mb} ["]
$5 \rightarrow 4$	90.772	OSO	0.61	42.0
$6 \rightarrow 5$	108.924	OSO	0.48	35.0
$12 \rightarrow 11$	217.817	JCMT	0.69	21.5
$19 \rightarrow 18$	344.779	APEX	0.73	17.5
		JCMT	0.62	14.0
$20 \rightarrow 19$	362.906	APEX	0.73	17.3

Table 3.4: The telescopes estimated main beam efficiency and beam width.

intensities are presented in table 3.3. The uncertainty in the intensity, that is estimated to be $\pm 20\%$, is dominated by the errors that are arising during the reduction of the data at the telescope and the conversion to the T_{mb} scale. The total intensity of the star V Cyg:s J = 5-4 transition was very difficult to derive because of its very low S/N. This line's relative uncertainty in its intensity was therefore set to be $\pm 50\%$. CW Leo had two observations of the rotational transition J = 5-4, taken by the OSO 20 m telescope. Therefore an average of the two spectra was done so that a better estimate, with a higher signal to noise ratio, of the lines intensity could given.

An upper limit of the intensity can be estimated for the stars where no detection were done of SiS in their spectrum. The upper limit of the intensity I_{upper} is given by formula 3.1,

$$I_{upper} = T_{pp} 2 v_e \tag{3.1}$$

where T_{pp} is the peak to peak value of main beam efficiency temperature T_{mb} after the resolution has been degraded to twice the expansion velocity v_e. The upper limits are presented in table 3.3 as $< I_{upper}$.

Chapter 4

Calculating the fractional abundances of SiS

The major aim of this diploma thesis is to calculate circumstellar abundances of SiS and look for possible correlations with the photospheric C/O-ratio and the mass loss rate of the star. These goals will be reached with the help of observations of some of the rotational transitions of the SiS molecule supplemented by a detailed excitation analysis, which in turn requires a reliable physical model. From the radiative transfer model it is possible to calculate line intensities that can be directly compared to the observed lines. A good fit will give the best estimates of the input parameters that are used in the model. In this section the model will be described, which types of approximations that are made and how it can be used to calculate the SiS fractional abundances. The SiS fractional abundance is defined as the ratio between the SiS abundance $\equiv$ number density and the H_2 abundance. SiS abundance, is sometime used as a shortening to the SiS fractional abundance.

One of the first things the model must be able to do is to calculate the excitation of the SiS molecules, ie., the level populations n_i. This would be rather easy to do if the CSE could be described to be in LTE (local thermodynamic equilibrium), where the relative level populations are determined only by the local kinetic temperature of the gas through the Saha and Boltzmann equations. However this is, as will be shown, generally not a good approximation for CSEs. A detailed non-LTE excitation analysis is therefore required.

The calculated level populations n_i will then be used to calculate the intensity that is emitted from the region where the SiS molecules are located. It is then possible to estimate how the lines would look if they were observed from earth. This part is also included in the model and the resulted modelled lines will then be compared to the observed ones.

All analysis of the data is performed using a radiative transfer package developed by F. Schöier. The package is divided in three different parts, each representing a certain phase in the modelling work. The three different parts of the program have each its own input file and they are executed one at each time after each other using the results from the first one in the second one and so on. The three different major parts are:

- Non-LTE excitation analysis.

  - The Monte Carlo code.
  - The input parameters.

- Estimating the modelled lines.
  - Solves radiative transfer equation, by integration along different lines of sight.
  - From n_i to T_{mb}.

- Plotting and χ^2 analysis.

The underlying physical model that is used is called the standard model, which means that certain approximations are done to describe the morphology of the CSE. The most important approximations in this model are: the mass loss rate ($\dot{M}$) is assumed to be isotropic and constant with time, the expansion velocity (v_e) of the CSE is set to be constant and the CSE:s geometry is taken to be spherically symmetric. The different parts of the program will be explained in more detail and their results will be presented in the following sections.

4.1 Non-LTE excitation analysis

The level populations n_i can be calculated with a non-LTE excitation analysis. This can be done with different types of radiative transfer codes, the one used in this diploma thesis project is based on the Monte Carlo Method, see Bernes at al. (1979) and Schöier et al. (2001). The Monte Carlo method is chosen because it has advantages like, it is easy to adapt so that new physical complications can be introduced, it is not too far from the physics, and it is rather easy to expand to be able to treat a wide variety of physical geometries. Examples of physical complications are for example inhomogeneities in the CSE and deviations from the spherically symmetric approximation which today is not included in the model. One disadvantage is that the program has a slow convergence ($\sqrt{N_{iter}}$), especially at larger optical depths. This is however not concerning this project because the lines of interest here are all rather optically thin. A comparison between different radiative transfer programs and their reliability can be found in van Zadelhoff et al. (2002).

4.1.1 The Monte Carlo method

The basic idea with the Monte Carlo method is that the radiation field is represented by a smaller amount of model photons. Each model photon will be emitted through the region of interest, in this case the CSE, where all its absorptions will be calculated by a counter. All the model photons will be studied like this until they have either been totally absorbed or left the CSE. The counter will give the total amount of absorptions in the CSE during a certain time that then can be used to solve the SE-equations, see eq. 2.15, that will give the new number of SiS molecules in each excited rotational level. The new level populations will then be used to calculate a new set of model photons that will be sent out and followed through the CSE. This will continue until the difference between the old and new level populations are reaching the convergence condition that has been set up. When this is fulfilled the level populations are determined

well enough for estimating the source functions that will be used in section 4.2 to calculate the modelled lines.

4.1.2 The input parameters

A number of input parameters, that are specific for each star and its circumstellar envelope, are needed to run the radiative transfer program so that estimations of their level populations n_i can be derived. The most important of these parameters, such as the mass loss rate, expansion velocity and radius of the SiS emitting envelope will be described here. The set of parameters adopted for each star can be found in table 3.2 in chapter 3.

Luminosity

All of the sample stars are Mira variables or semi-regular variables which means that their luminosity can be related to their period, see Whitelock et al. (1994), Groenwegen & Whitelock (1996). This correlation is described by the period-luminosity relation by the empirical formulas 4.2 and 4.1, which are used to calculate the absolute luminosity of the stars, see Gonzales Delgado et al. (2003) and Schöier et al. (2006).

Carbon stars:

$$M_{bol} = 2.02 - 2.59 logP \tag{4.1}$$

M-type stars:

$$M_{bol} = 2.80 - 3.00 logP \tag{4.2}$$

where P is the period in days and M_{bol} is the bolometric absolute magnitude.

The distance, stellar temperature, dust's optical depth, $T_{\rm dust}(r)$, and the condensation radius r_i

The most accurate measurements of the distances to stars is done by the Hipparcos Satellite (High Precision Parallax Collecting Satellite) that was launched in 1989. The satellite measured the parallaxes of the stars which then is used to calculate the distances. Unfortunately, the Hipparcos satellite did not measure any parallaxes for this project's sample of stars, they were not bright enough, so the distances had to be estimated from the P-L relations.

For this sample of stars the distances were estimated from best fit models of the stars observed SED (spectral energy distribution) through detailed dust radiative transfer modelling, see Fig. 4.1. In the modelling also the dust's optical depth, the stellar temperature and the dust condensation radius r_i were derived. For a more detailed description see Schöier et al. (2002) and Schöier et al. (2006). This type of calculation of the distance has usually a relative error of about 50%, but it is today the best estimate of the distances that can be obtained for the objects that are studied in this project. The distances, dust optical depths, stellar temperatures and dust condensation radii are taken from Schöier et al. (2006) and Schöier et al. in prep. In addition, the radial distribution of the dust grains temperature is obtained from the SED modelling and used in the molecular excitation analysis.

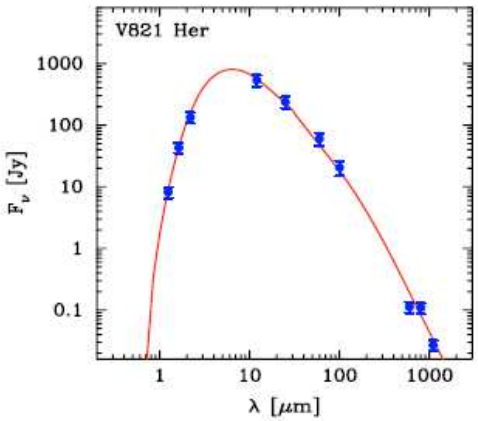

Figure 4.1: The best fit model of the carbon star V821 Her's SED taken from Schöier et al. (2006).

The mass loss rate and expansion velocity from CO modelling

The mass loss rates and expansion velocities are calculated from modelling of CO line emission. The mass loss rates will have absolute errors of a maximum factor of three or less. The error is coming from the uncertainties in the distance but also from other parameters that are used in the model to estimate the mass loss rates. One aspect that also is important to have in mind when interpreting the results is that the mass loss rates are estimated from multi transition modelling of low excitation CO lines, typically J = 1-0 up to J = 3-2 or 4-3, which are predominantly probing the more external part of the CSE compared to SiS line emission. This is due to their different spatial distributions of their CO envelopes that are about ten times larger than the SiS line emitting envelopes. This will not affect the results when the mass loss rate is not varying so much in time. However, recent studies have proven that some stars have rather strong time variations of the mass loss rates (see the review article by Schöier 2007). The mass-loss rates and expansions velocities have been taken from Gonzales Delgado et al. (2003), Olofsson et al. (1997), and Schöier et al. (2006).

The CO lines are very often used when estimating the physical conditions in CSEs. The reason for this is that the CO lines are generally the strongest lines that are emitted from AGB's CSEs, which is important when using them in modelling. The CO lines are strong because the CO molecules are after H_2 usually the most abundant species, they are difficult to photodissociate and easy to excite.

The photodissociation radius

The photodissociation radius , which is the size of the SiS-line emitting envelope, can be estimated from the empirical formula 4.3 taken from Gonzales Delgado et al. (2003).

$$\log(r_e) = 19.2 + 0.48 \log\left(\frac{\dot{M}}{v_e}\right) \tag{4.3}$$

The SiS-line emitting envelopes are approximated to be the same as the ones that have been used in the models to calculate the abundances of SiO. The approximation can be done because of the many similarities between the molecules and the assumption that they should react similarly to photodissociation and condensation.

Molecular data

Molecular data are taken from Schöier et al. (2005) and are publically available at (www.leidenuniv.nl/∼moldata) Leiden Atomic and Molecular Database (LAMDA). It includes energy levels up to SiS J = 40 in both the v = 0 and v = 1 vibrational states. The collisional rate coefficients SiS-H_2 where taken to be the same as for SiO-H_2, (see Schöier et al. 2005).

4.2 The modelled lines

The second part of the radiative transfer program will from the level populations calculate the intensity for each line from the SiS line emitting region. It will also estimate how this line changes when it is passing through the CSE and the interstellar medium all the way to earth where it will be observed. The resulting modelled line will be plotted and compared to the observed line. A more detailed description of the procedure will be given below.

The program will first start with calculating the source function (see eq. 2.14) for each line from the level populations that were calculated in the first part of the radiative transfer program. The source function can then be used to estimate the intensity for the line, see the radiative transfer eq. 2.5. The intensity is then describing how the line would look if it would be observed directly outside the star. The brightness distribution can then be convolved with appropriate beams to simulate a real observation. This is why the beam width for each telescope must be included in the input-file. The observed line intensities, that the modelled lines will be compared with, are already corrected for the atmospheric effect on the lines. Other important parameters, in the input-file, are the distance to the star and the number of lines of sight that the radiation transfer equations are using when calculating the lines intensities.

The beam widths, see table 3.4, were calculated exactly the same way as the main beam efficiency that were described in section 3.5.2. They are also specific for each telescope and wavelength. The values that were used in the calculations, were taken from the telescope's homepages.

4.3 SiS abundances and χ^2

The estimated modelled lines will be compared to the observed spectra lines in the last part of the modelling procedure. This is done by calculating the total χ^2_{tot} between the model and the data with equation 4.4,

$$\chi^2_{tot} = \sum_{i=1}^{N} \frac{(I_{model,i} - I_{obs,i})^2}{\sigma_i^2} \tag{4.4}$$

where $I_{model,i}$ is the integrated intensity for a specific line given by the model, $I_{obs,i}$ is the integrated intensity of the same line taken from the observations, N is the number of observed lines and σ_i is the absolute error in the observed intensity.

The abundance of SiS will be adjusted until a minimum χ^2_{tot} is found. In this way will the SiS abundance be used as the single parameter that is varied in the model until a good fit is reached. The best fit will in this way also give the best estimation of the SiS fractional abundances. The SiS abundance is changed in steps of 10%. The results from the best fit for each star are presented in section 4.4.2.

4.4 Results from the modelling

4.4.1 An example on how the results from the three steps in the model are presented

The best fit model of the star WX Psc is shown in Fig. 4.2 and Fig. 4.3 as an example of how the results from the estimation of the levels populations, modelled lines and the fitting between the modelled lines and the observed lines are presented. Here have 45000 model photons and four observed rotational transitions: J=5-4, 6-5, 12-11 and 19-18, been used.

Figure 4.2, results from the best model of WX Psc

The first figure at the top corner to the left is summarizing the most important parameters that have been used and/or calculated in the model. The next three figures to the right of the first one is showing that the number density of H_2, the fractional abundances of SiS and the kinetic temperature of the gas is going down, as expected, with the radius in the model.

The four diagrams in the middle are plotting how the excitation temperature (solid line) is changing in relation to the kinetic temperature (dashed line) with the radius of the star for each rotational transition. LTE would have been a good approximation if the excitation temperature would have been close to the value of the kinetic temperature throughout the CSE. This is not the case, which is motivating the use of a non-LTE radiative transfer code. The excitation temperature is instead going above the line (super-thermally excited) for the lower transitions and below it (sub-thermally excited) for the higher rotational transitions. All of the stars are showing similar types of differences between the rotational transitions, even though not always such big differences as shown here. It is therefore very interesting to see that this relation will change when the dust is excluded from the model in section 5.2.

The four last diagrams are describing how the normalized excitation temperature is varying with each iteration for a certain amount of given rotational transitions. The figures are showing that the normalised excitation temperature is approaching one after just a few iterations, i.e., convergence of the level

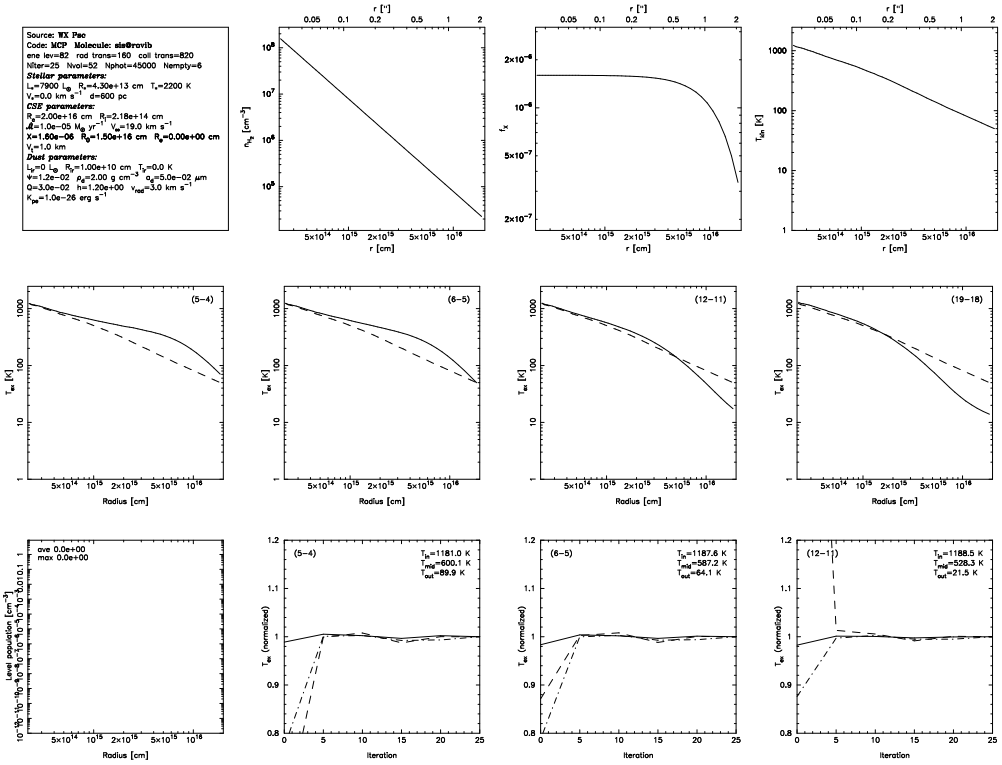

Figure 4.2: Results from the best model for WX Psc.

populations is fast. This is indicating that the model is efficient to use when calculating the level populations for the SiS molecules.

Figure 4.3, The modelled and observed lines

In Fig. 4.3 can the best resulted modelled lines be seen for the SiS rotational transitions: J = 5-4 and 6-5 in red and the observed lines presented in histograms in black. Similar figures are plotted for all the stars lines together with the total chi squared after each run by the model.

4.4.2 The SiS fractional abundances

The derived abundances of SiS are presented in table 4.1 together with their calculated χ^2_{red}, that is taken account of the number of free parameters that are used in the modelling, see equation 4.5.

$$\chi^2_{red} = \frac{\chi^2_{tot}}{d} \tag{4.5}$$

where d is the number of degrees of freedom:

$$d = N - c \tag{4.6}$$

and N is the number of lines and c the number of constraints, which in this case is the number of varying parameters in the model.

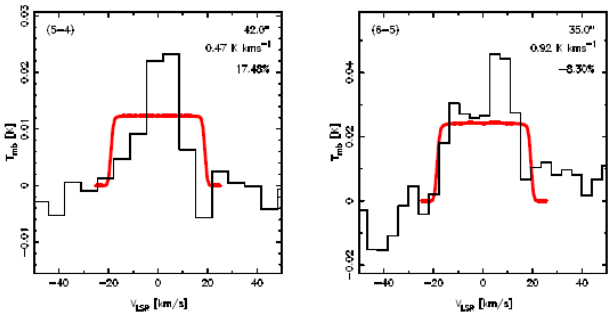

Figure 4.3: Results from the best model for WX Psc. To the left is the SiS J = 5-4 and to the right the SiS J = 6-5. The lines are observed by OSO.

The error estimation of the derived SiS abundances is very complicated. The uncertainty of 20% in the intensity from the observations can be directly propagated to introduce a relative error of 20% in the SiS abundances. This error is however much too small to cover the uncertainties in the modelling of the lines.

The errors from many of the different input parameters will affect the results from the modelling in very complicated ways that can not be easily derived. For further discussion see Gonzales Delgado et al. (2003). There they varied many of the parameters to see how this would affect their results of the SiO abundances and they concluded that the errors were about a factor of 3-5 depending on which mass loss rate the star had. These results are considered to be adaptable on this projects SiS abundances error estimation. This conclusion was based on the fact that the same model was used, with parameters of the same orders and that the molecules SiO and SiS have several similar properties. The uncertainty in the SiS abundances is therefore estimated to about a factor of three within the adopted circumstellar model.

The median value of the SiS abundances for the carbon stars is $2.5 \cdot 10^{-6}$, with the maximum value of $5.5 \cdot 10^{-6}$ and the minimum value of $1.0 \cdot 10^{-6}$. The M-type stars have a median of is $2.1 \cdot 10^{-7}$, with the maximum value of $1.6 \cdot 10^{-6}$ and minimum value of $3.5 \cdot 10^{-8}$. They are also plotted in Fig. 4.4 against their $\dot{M}/v_v$ ratio, which is a form of density measurement, on the x-axis. These results are clearly showing that the carbon stars have a factor of around 10 higher SiS abundances than the M-type stars. The carbon stars median value are agreeing rather well with the most recent chemical models while the M-type stars have factor of 10-100 higher than what the most recent chemical models are predicting, see Cherchneff et al. (2006). This is further discussed in section 6.2.

The SiS abundance also shows a tendency to decrease when the mass loss rate is increasing, this is especially clear when studying the carbon stars. The correlation between the mass loss rate and the SiS abundance was derived with the correlation function that gives the correlation value r, see eg. 4.7. If the correlation value r is above 0.6 then this is indicating that there is a strong correlation between the SiS abundance and the mass loss rate.

Source	IRAS	$\dot{M}$ [$M_\odot$ yr^{-1}]	v_e [km s^{-1}]	r_e [cm]	f_{SiS}	χ^2_{red}	N[a]
M-stars:							
GX Mon	06500 + 0829	$2.0{\cdot}10^{-5}$	18.0	$2.2{\cdot}10^{16}$	$9.0{\cdot}10^{-8}$	5.7	3
IK Tau	03507 + 1115	$1.0{\cdot}10^{-5}$	18.0	$1.6{\cdot}10^{16}$	$8.5{\cdot}10^{-8}$	10.9	4
IRC-10529	20077 - 0625	$2.5{\cdot}10^{-6}$	11.0	$1.0{\cdot}10^{16}$	$2.0{\cdot}10^{-7}$	9.3	3
IRC+40004	00042 + 4248	$6.0{\cdot}10^{-6}$	17.5	$1.3{\cdot}10^{16}$	$3.5{\cdot}10^{-7}$	...	1
IRC+50137	05073 + 5248	$1.0{\cdot}10^{-5}$	16.5	$1.6{\cdot}10^{16}$	$2.2{\cdot}10^{-7}$	1.6	2
R Cas	23558 + 5106	$1.1{\cdot}10^{-6}$	8.0	$0.8{\cdot}10^{16}$	$1.5{\cdot}10^{-7}$	...	1
TX Cam	04566 + 5606	$7.0{\cdot}10^{-6}$	18.0	$1.3{\cdot}10^{16}$	$4.5{\cdot}10^{-7}$	4.0	3
WX Psc	0137 + 1219	$1.0{\cdot}10^{-5}$	19.0	$1.5{\cdot}10^{16}$	$1.6{\cdot}10^{-6}$	0.4	4
C-stars:							
CW Leo	09452 + 1330	$1.5{\cdot}10^{-5}$	14.0	$2.2{\cdot}10^{16}$	$1.4{\cdot}10^{-6}$	3.1	3
LP And	23320 + 4316	$1.5{\cdot}10^{-5}$	13.5	$2.2{\cdot}10^{16}$	$1.0{\cdot}10^{-6}$	5.4	2
RV Aqr	21032 - 0024	$2.8{\cdot}10^{-6}$	15.0	$9.3{\cdot}10^{15}$	$1.3{\cdot}10^{-6}$	...	1
RW LMi	10131 + 3049	$6.0{\cdot}10^{-6}$	16.5	$1.3{\cdot}10^{16}$	$3.5{\cdot}10^{-6}$	4.1	2
V Cyg	20396 + 4757	$9.0{\cdot}10^{-7}$	10.5	$6.4{\cdot}10^{15}$	$3.0{\cdot}10^{-6}$	...	1
V384 Per	03229 + 4721	$3.5{\cdot}10^{-6}$	14.5	$1.1{\cdot}10^{16}$	$2.5{\cdot}10^{-6}$	...	1
V821 Her	18397 + 1738	$1.8{\cdot}10^{-6}$	13.0	$8.1{\cdot}10^{15}$	$5.5{\cdot}10^{-6}$	...	1
15082-4808	15082 - 4808	$1.0{\cdot}10^{-5}$	19.0	$1.5{\cdot}10^{16}$	$2.5{\cdot}10^{-6}$	9.9	3
15194-5115	15194 - 5115	$9.0{\cdot}10^{-6}$	21.0	$1.4{\cdot}10^{16}$	$1.9{\cdot}10^{-6}$	16.1	3

[a]Number of lines

Table 4.1: Results from modelling.

$$r = \frac{\sum_i (x_i - \bar{x})(y_i - \bar{y})}{\sqrt{\sum_i (x_i - \bar{x})^2}\sqrt{\sum_i (y_i - \bar{y})^2}} \tag{4.7}$$

The calculation of the r-value for the M-type stars relative the mass loss rate was about 0.03, which concludes that no clear correlation between them could be found. The r-value for the carbon stars SiS abundances were around -0.6 relative both the mass loss rate and the $\dot{M}/v_e$ ratio, although still for a rather small number of sources. This is showing that there is a strong correlation between the SiS abundances and the mass loss rates of the carbon stars.

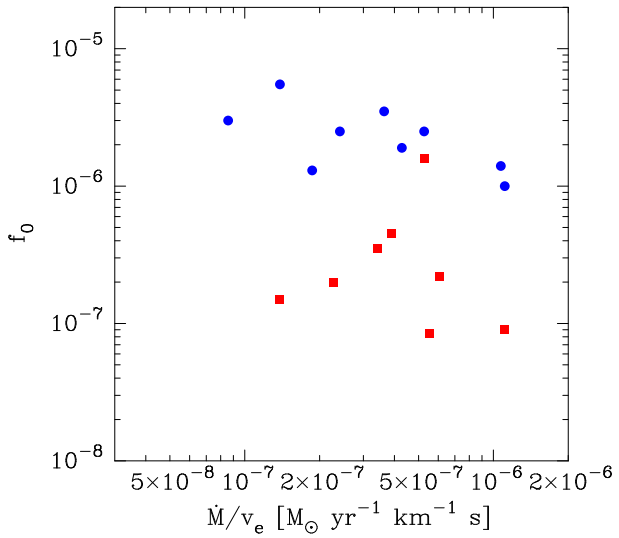

Figure 4.4: The resulted SiS abundances from the modelling plotted against the $\dot{M}/v_e$. The red dots are the M-type stars and the blue dots the carbon stars.

Chapter 5

Testing the model to learn more about the SiS results

5.1 A compact component

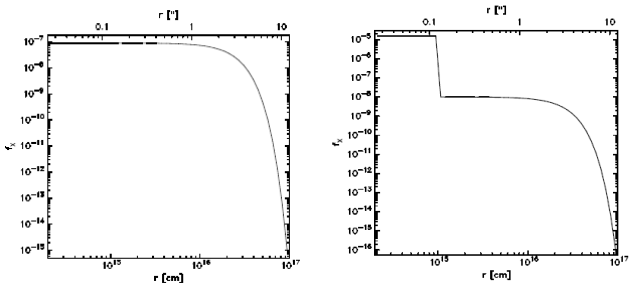

(a) The SiS abundances variation with radius for GX Mon

(b) The SiS abundances variation with radius for GX Mon, with a compact component included in the model.

Figure 5.1: The results from modelling of GX Mon with and without a compact component included in the model.

8 AGB stars were chosen to be remodelled with a compact component included in the model to see how this might improve the fits between the modelled and observed lines. Of these 8 stars were 5 M-type stars and 3 carbon stars. They were chosen because they had 3 or more observed SiS emission lines, which were the lower limit of the number of observed lines that were required to calculate a χ^2_{red} with two free parameters. The two free parameters that were varied in the model with a compact component were f_0, the SiS abundance, and f_c, the SiS abundance in the compact component. The inner condensation radius r_c, where the compact component ends, is fixed to $1.0 \cdot 10^{15}$ cm for all the stars. The differences between the model with a compact component and a model without

a compact component can be seen in Fig. 5.1. The two abundance parameters where varied until a best fit between the modelled lines and the observed emission lines were reached. The results can be seen in table, 5.1. Two stars, GX Mon's and IK Tau's, χ^2_{red} improved from 10.9 to 2.5 and from 5.7 to 1.4 respectively, with a compact component in the model. The compact component also resulted in smaller SiS abundances in these two stars. The other stars fits did not improve in any higher extent.

Source	GX Mon IK	Tau	IRC-10529	TX Cam
χ^2_{red}	5.7	10.9	7.3	4.0
χ^2_{red}(comp)	1.4	2.5	x	x
f_0	$9.0{\cdot}10^{-8}$	$8.5{\cdot}10^{-8}$	$2.5{\cdot}10^{-7}$	$4.5{\cdot}10^{-7}$
f_0(comp)	$1.0{\cdot}10^{-8}$	$< 5.0{\cdot}10^{-9}$	x	x
f_c	$1.5{\cdot}10^{-5}$	$9.0{\cdot}10^{-6}$	x	x
Source	WX Psc	CW Leo	IRAS15082	IRAS15194
χ^2_{red}	1.3	4.8	6.3	12.9
χ^2_{red}(comp)	x	x	x	x
f_0	$1.6{\cdot}10^{-6}$	$1.4{\cdot}10^{-6}$	$3.6{\cdot}10^{-6}$	$3.0{\cdot}10^{-6}$
f_0(comp)	x	x	x	x
f_c	x	x	x	x

Table 5.1: Results from remodelling with compact component included in the model.

The common thing for IK Tau and GX Mon is that they both have a low SiS abundance $\approx 10^{-7}$, see table 4.1 To see how sensitive the SiO and SiS emission lines are to a model with and without a compact component included additional tests were made. In this test a model for a star with a specific set of stellar and circumstellar parameters was executed with and without a compact component. The ratio between the line intensity I_{comp} from a model with a compact component included and the intensity I from a model without the compact component included was then calculated for each specific line of interest. This I_{comp} / I ratio was then calculated for different mass loss rates, SiS and SiO abundances, see Fig. 5.2. Clearly the SiS line intensities, as well as the ratios, are more sensitive to abundance gradients than those of SiO. These results will be further discussed in section 6.

5.2 A test of the most contributing source to SiS line excitation

The two main sources of excitation of the SiS molecules in this sample of objects, in addition to collisions with H_2 molecules, are the luminosity from the star and the dust emission. The photons of the star are mainly absorbed by the gas and dust before they have a chance to reach the SiS line emitting region, especially if it is a high mass loss rate star because of it is higher densities of gas and dust. This does not mean that the stars luminosity is not affecting the line emission at all. Some of the photons will reach the SiS line emitting region and many of the photons will also be absorbed by the dust and remitted at longer wavelengths, with a maximum at around 8 μm, that will affect the SiS lines. So the dust is not just absorbing photons it is also emitting them. This might have an important influence on the different line intensities. A few tests have been

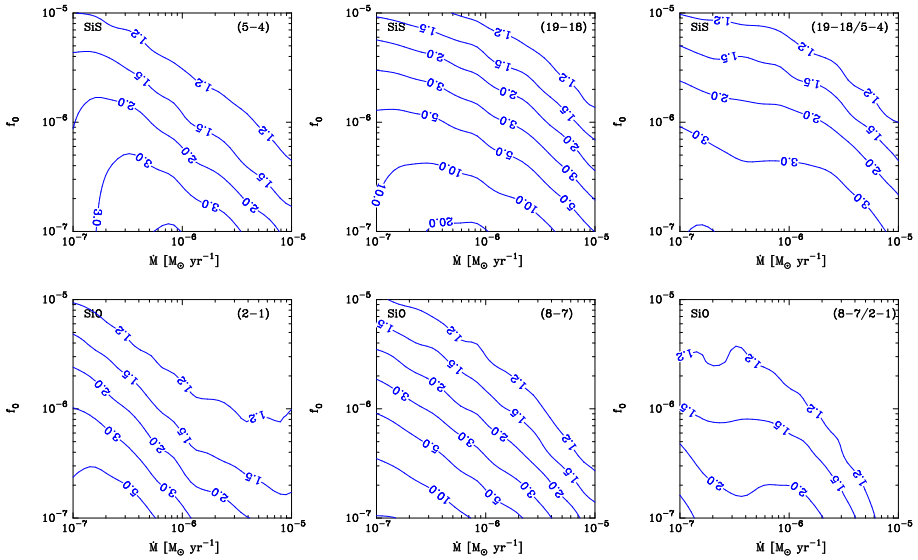

Figure 5.2: Results from calculating how the ratio I/I_{comp} is changing with the SiS and SiO abundances and with the mass loss rate. This is done for a model star with: $v_e = 12$ km/s, $L = 6000\ L_{\odot}$, $T_{\star} = 2400$ K, $\tau_{10} = 0.1$, $f_c = 2.0{\cdot}10^{-5}$ and $r_c = 1.0{\cdot}10^{15}$. The T_{kin}(r) and T_{dust}(r) are set to be the same as for the star R For.

performed to see how each of these sources are contributing to the excitation of the SiS-molecules and if the lines intensities are affected differently by them.

The tests estimated how the different line intensities change when the star is turned off, the dust is taken away and when both the dust is taken away and the star is turned off. The stars under study were: IRC-10529, WX Psc and CW Leo. WX Psc and CW Leo were chosen because they both have high mass-loss rates in each of the groups of M-type stars and carbon stars. IRC-10529, which is a M-type star was chosen because of its low mass loss rate. The sample of stars was also chosen because these stars have observations of 3 to 4 rotational transitions each and all transitions is represented so that differences between the lines can be studied. All models have been done with 45000 model photons. The results can be seen in table 5.2.

The results clearly show that the luminosity of the star is not affecting the line intensities in the high mass loss rate stars to any higher extent. This was also expected because of their higher densities of H_2 that will absorb most of the photons from the star irrespective of if there was dust there or not. It can therefore be seen that an increased luminosity in the lower mass loss rate star IRC-10529 will increase all of its line intensities just because of the higher rate of photons that can reach and excite the molecules.

The results also indicate that the dust is a very important factor in the excitation of SiS molecules. The integrated line intensities are increasing with a factor of 2 or more for the higher rotational transitions J = 12-11, 19-18 and 20-19, when the dust is included in the model. The highest factor is seen in the star IRC-10529 which has the lowest mass-loss rate. An interesting thing to note here is that both the star, IRC-10529 and WX Psc have higher line

Model with	I_{mb}[a] [K km s^{-1}]				
	$5 \rightarrow 4$	$6 \rightarrow 5$	$12 \rightarrow 11$	$19 \rightarrow 18$	$20 \rightarrow 19$
M-stars:					
IRC-10529					
star + dust	0.25		0.96	1.27	
dust	0.17		0.85	1.10	
star	0.48		0.58	0.54	
no star or dust	0.37		0.36	0.32	
WX Psc					
star + dust	0.47	0.92	4.10	3.78	
dust	0.47	0.91	4.08	3.75	
star	0.72	1.12	2.15	1.85	
no star or dust	0.70	1.07	2.06	1.79	
C-stars					
CW Leo					
star + dust	40.1	69.2			127.3
dust	40.0	69.0			125.9
star	38.4	53.7			63.6
no star or dust	35.6	50.0			61.8

[a]Modelled intensity

Table 5.2: The different sources for line excitation

intensities for the lower rotational transitions when the dust is taken away than when it is included. These results are also agreeing rather well with the ones in Schöier et al. (2006) where a similar study has been done for the SiO molecule. It is shown there that in the case of high mass loss rate objects dust is playing a more important role than the emission from the star, especially for the higher transitions.

5.2.1 The importance of inclusion of dust in the model.

As has been shown earlier, from the results of the modelling, the excitations temperatures for the different rotational transitions are sensitive to how the different parameters are varying in the model and also with the radius of the star. The excitation temperatures are not at all affected by changes in the stellar parameters but they were all decreased to below the kinetic temperature at higher radii when the dust was excluded from the model (see Fig. 5.3). An explanation for this could be the loss in temperature and line emission. The higher rotational transitions are not affected by this as much as the lower rotational transitions, as can be seen in Fig. 5.3 when comparing it with Fig. 4.2. They decouple from $T_{\rm kin}$ at smaller radii. So dust emission is able to maintain excitation further out.

There are many other different factors that are dependent of the dust, that could explain the changing line intensities. The line intensities might both increase because of the smaller optical depth when the dust is taken away or decrease because of the absence of photons that are emitted from the dust. The size of emitting region might also change because of the much smaller or bigger amount of dust grains. If the SiS line emitting region will be smaller for some of the SiS rotational transitions that will then lead to that their intensities will be lowered because of the dilution by the beam of the telescope.

One other very important aspect to have in mind is that the distribution of photons will change. The peak of the distribution of photons will for example

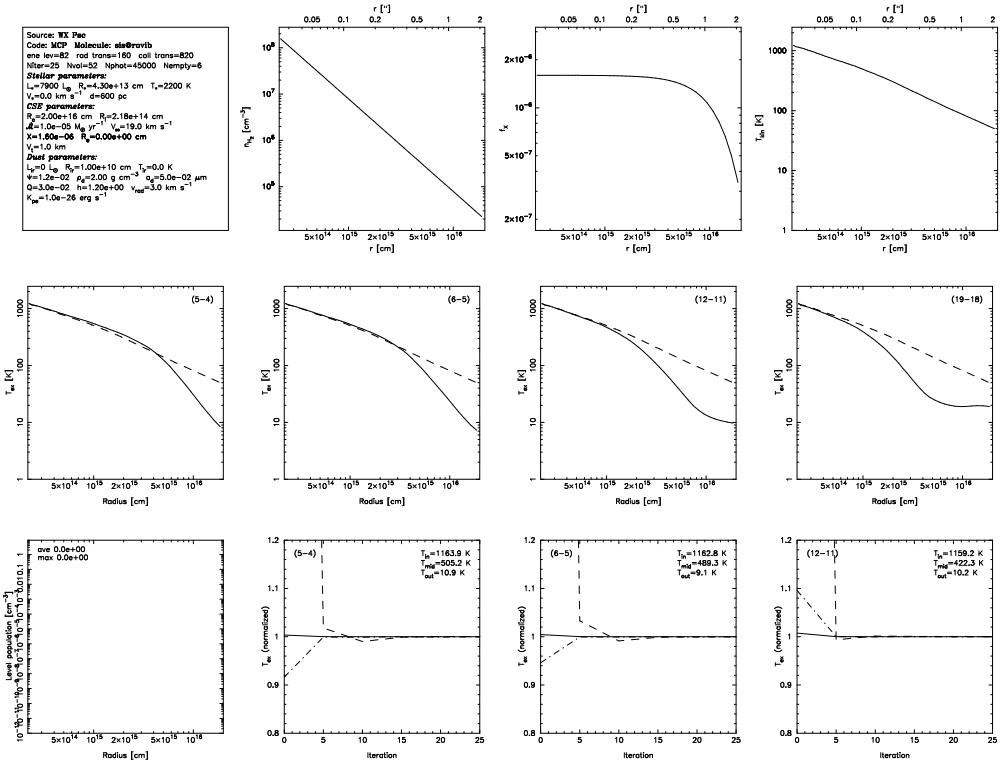

Figure 5.3: Results from the best model for WX Psc when the optical depth is put to zero. This means that the dust is excluded from the model.

be moved to higher energies when dust is not included in the model because of the absences of dust grain that can absorb them and then reemit them of lower frequencies. This might explain the decrease of the line intensities in the lower transitions and the increase in the higher transitions when dust is included in the model and the other way around depending on where the peak of the distribution of photons will be.

The most significant conclusion that can be taken from this study is that the dust has a bigger impact on the line intensities than the stellar parameters and that it is therefore very important to include the dust in the models. If the dust would not have been included in the models an increase of the fractional abundances of SiS would have been needed to compensate for the loss of emission related to the dust for some of the stars, which would have given wrong estimates of the SiS fractional abundances.

Chapter 6

Discussion

6.1 Carbon stars versus M-type stars

6.1.1 Comparison with earlier research on SiS

The results clearly show that it is a higher fractional abundance of SiS in carbon stars than in M-type stars. These results are interesting to compare with the results by Woods et al. (2003) and Bujarrabal et al. (1994), see table 6.1. The median value of the SiS abundance for the carbon stars from Woods et al. (2003) is $2.7{\cdot}10^{-6}$ which is very close to the estimated median SiS abundance $2.5{\cdot}10^{-6}$ from this diploma thesis project. It is important to have in mind when interpreting this that the intensities from Woods et al. where used in the models when deriving the SiS abundances. This might have influenced the results to be a bit closer to eachother, but it is still interesting to see that they are so similar. Because the model used in Woods et al. are less complex than the ones used in this diploma thesis and they have also just used one SiS line when deriving the abundance. The comparison between SiS abundances taken from Bujarrabal et al. with the results from this project show that they also derived SiS abundances for the M-type stars that are about a factor of ten lower than the abundances in the carbon stars. Intensities from Bujarrabal et al. were not used in this projects models, beside in one star. The major difference between their and this diploma thesis SiS abundances is that their abundances is in general higher for both M-type stars and carbon stars.

This divergence can be explained by the use of different distances, mass loss rates, and sizes of the SiS emitting envelopes in the models. Bujarrabal et al have also used a LTE as an approximation, while non-LTE has been used in this project to derive the abundances. Non-LTE is today considered to be a better description of the environment in CSE because of its low densities and lower temperatures, but this is also demanding a more complicated radiative transfer program. The use of LTE is making the results much more sensitive to the SiS emitting envelopes size, which could be one of the most important explanations for the difference in the results.

One other very important difference is also that Bujarrabal and Woods et al. have just been using one rotational transition in there models when up to 4 lines have been used in this diploma thesis. It is very legible from this project's high χ^2_{red} that one should be very careful when using just one rotational transition

when estimating the SiS abundances.

Source	IRAS	f_{SiS} W.-03	f_{SiS} B.-94	f_{SiS} Dipl.Th	χ^2_{red}	N[a]
M-stars:						
GX Mon	06500 + 0829			$9.0{\cdot}10^{-8}$	5.7	3
IK Tau	03507 + 1115		$4.4{\cdot}10^{-7}$	$8.5{\cdot}10^{-8}$	10.9	4
IRC-10529	20077 - 0625		$5.6{\cdot}10^{-7}$	$2.0{\cdot}10^{-7}$	9.3	3
IRC+40004	00042 + 4248			$3.5{\cdot}10^{-7}$	...	1
IRC+50137	05073 + 5248			$2.2{\cdot}10^{-7}$	1.6	2
R Cas	23558 + 5106			$1.5{\cdot}10^{-7}$	...	1
TX Cam	04566 + 5606		$1.5{\cdot}10^{-6}$	$4.5{\cdot}10^{-7}$	4.0	3
WX Psc	0137 + 1219			$1.6{\cdot}10^{-6}$	0.4	4
C-stars:						
CW Leo	09452 + 1330	$9.5{\cdot}10^{-7}$	$3.9{\cdot}10^{-6}$	$1.4{\cdot}10^{-6}$	3.1	3
LP And	23320 + 4316	$9.5{\cdot}10^{-7}$	$3.5{\cdot}10^{-6}$	$1.0{\cdot}10^{-6}$	5.4	2
RV Aqr	21032 - 0024			$1.3{\cdot}10^{-6}$	...	1
RW LMi	10131 + 3049	$3.1{\cdot}10^{-6}$	$1.9{\cdot}10^{-6}$	$3.5{\cdot}10^{-6}$	4.1	2
V Cyg	20396 + 4757		$7.4{\cdot}10^{-7}$	$3.0{\cdot}10^{-6}$	...	1
V384 Per	03229 + 4721			$2.5{\cdot}10^{-6}$	...	1
V821 Her	18397 + 1738			$5.5{\cdot}10^{-6}$	...	1
15082-4808	15082 - 4808	$2.7{\cdot}10^{-6}$		$2.5{\cdot}10^{-6}$	9.9	3
15194-5115	15194 - 5115	$4.6{\cdot}10^{-6}$		$1.9{\cdot}10^{-6}$	16.1	3

[a]Number of lines

Table 6.1: Results from the diploma thesis project(Dipl.Th) in comparison to the results from Woods et al. (2003) (W.-03) and from Bujarrabal et al. (1994) (B.-94)

6.1.2 What do the chemical models say

It is also very interesting to compare the results with the SiS abundances that have been derived from the chemical models. The chemical model used in Cherchneff et al. (2006) is deriving a higher distinction between the SiS fractional abundances in M-type stars and the carbon stars than is estimated from the observations in this diploma thesis project. There are many arguments that could be used to explain this difference. One of these are that the chemical models is estimating the molecular abundances a few stellar radii from the center of the star whereas the observations is deriving the abundances a couple of hundred stellar radii from the center of the star.

The estimated abundances with the observations is also a lower limit of the abundance because some of the SiS molecules might have been depleted onto dust grains which will decrease the real value of the observed abundances. This would in fact speak for a even bigger difference between the chemical models and the observations, because then would the observed abundances in the M-type stars be even higher than they are estimated to be now.

One other reason, for the divergence between the chemical models and observations, can be that the chemical reactions that produce SiS are not set to be as efficient in the chemical models as they should be according to the observations. In the article Duari et al. (1998) where the SiS abundance calculated in the star IK Tau with a similar chemical model that Cherchneff later used. They estimated it to be around $3.8{\cdot}10^{-10}$ but it is varying a lot with the radius.

This is much lower than the estimated value $8.5 \cdot 10^{-8}$ in this project.

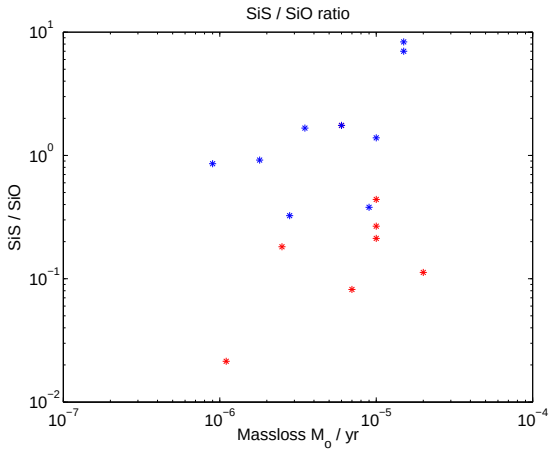

Figure 6.1: The SiS/SiO ratio for all the stars in the sample

6.1.3 The SiS results relative to results for SiO

The ratio SiS/SiO has been calculated for all of the sample's stars, see Fig. 6.1, to compare the derived SiS abundances with the SiO abundances. It can be seen in the figure that there is about the same amount of SiO as SiS in the carbon stars. There are though two stars, CW Leo and LP And, that are having much higher SiS/SiO ratios. These high ratios is mostly dependent on their very low SiO abundance that could be related to their high mass loss rates.

For the M-type stars is the SiS/SiO ratio mostly below one, which can be explained by the stars' low abundance of SiS. The largest difference between the estimated abundances of SiS and SiO in this same sample of stars was that carbon stars have much more SiS than M-type stars, while there was no clear divergence in the SiO abundance between the two different types of stars. This is clearly shown in Fig. 6.2. The SiO abundances for the carbon stars are taken from Schöier et al. (2006) and for the M-type stars from Gonzales Delgado et al. (2003). The difference in SiS, between the two types of stars, will be explained by chemical models in the next section.

6.2 The chemical models

The difference in the SiS abundance between the carbon stars and M-type stars can be explained by how strong the formation and destruction processes in the stars are. The following chemical reactions and discussion are taken from Cherchneff et al. (2006). The derived SiS abundances from the chemical models are plotted against the stellar radius for stars with different C/O ratio in Fig. 6.4. It is there clearly shown that it is a much higher amount of SiS in carbon stars than in M-type stars. It can also be seen there that the SiS abundance in carbon stars is rather constant with radius whereas the SiS abundance for M-type stars is decreasing with stellar radius. This decrease is explained by the low

abundance of Si-atoms at higher stellar radii in M-type stars, see Fig. 6.3(a), that will lower the efficiency in the formation reaction 6.1.

$$S + Si + M \rightarrow SiS + M \tag{6.1}$$

where M is a molecule that acts as an catalysator. This reaction is however more favoured in carbon stars because of their higher rates of free Si-atoms. The majority of free Si-atoms comes from reaction 6.2,

$$Si + OH \rightarrow SiO + H \tag{6.2}$$

where SiO is the one of the reactants. This reaction is going in both directions for both types of stars at lower radii. At higher radii is this changed. Most of the SiO atoms in M-type stars will then react further with oxygen to form SiO_2 that will bind the free Si atoms. This will not be done in the carbon stars because of their lower abundance of oxygen. This means that the SiO-Si reaction in carbon stars will continue to go both ways and in this way still be producing free Si-atoms. The other formation reaction 6.3 of SiO is favoured close to the stellar photosphere and it is as efficient in M-type stars as in carbon stars.

$$Si + HS \rightarrow SiS + H \tag{6.3}$$

There are also two major destruction reactions:

$$SiS + H \rightarrow Si + HS \tag{6.4}$$

$$S + SiS \rightarrow S_2 + Si \tag{6.5}$$

The first one, reaction 6.4 is most efficient just above the stellar photosphere and it is equally favoured in both M-type stars and carbon stars. The second SiS-destruction reaction 6.5, that is mostly occurring at larger stellar radii, is much stronger in the M-type stars than in the carbon stars because of the M-type star's higher rates of free S-atoms, see Fig. 6.3(b). This more efficient destruction reaction is one very important reason to the lower abundances of SiS in M-type stars. The higher abundance of sulphide in M-type stars is explained by the more efficient reaction 6.1 in carbon stars that consumes most of the sulphide. The reaction 6.6,

$$CS + O \rightarrow CO + S \tag{6.6}$$

that replenish the gas with atomic S is also much more efficient in M-type stars because of the higher amount of atomic oxygen.

6.3 Condensation onto dust grains

One of the two major goals with this diploma thesis project was to investigate how the SiS abundance is varying with the mass loss rates for carbon stars and M-type stars. The results that are presented in Fig. 4.4 in chapter 4 are showing a decrease in the SiS abundance in carbon stars when the mass loss rate is increasing. This is further supported by calculating the correlation value r =

-0.6, that clearly stated a strong negative correlation between the SiS abundance and the mass loss rate. Such a correlation where however not found between the mass loss rate and the SiS abundance for the M-type stars. The conclusion is therefore that SiS is condensed onto the dust grains more effectively at higher mass loss rates, where the densities are higher and thus the chance for adsorption is increased, for the carbon stars but that this could not be shown for the M-type stars. This can also be further proven by fitting a postcondensation function to the derived SiS abundances for the carbon stars. This function,

$$f_{SiS} = Ae^{-B\dot{M}} \tag{6.7}$$

,where A and B are constants, is describing the expected dependence for the postcondensation abundance according to a rather simple dust model (see Delgado et al, 2003 for an average AGB star). As can be seen in Fig. 6.5(a) is the fit not very good but the data show a tendency to follow the line. This could however, as expected, not be seen for the M-type stars, see Fig. 6.5(b).

There are many reasons for why the M-type stars do not show any clear tendency for a decrease in their SiS abundance at higher mass loss rates. One of the most important is that the range of mass loss rates are not so large. A decrease in the SiS abundance might have been seen if more M-type stars with lower mass loss rates had been observed and had SiS detected in them. This hypothesis can be supported with the same sample of stars results from the SiO observations. see Fig. 6.2(b). In this figure is the decrease in the carbon stars abundance also rather clear while it is not as clearly shown for the M-type stars. The decrease in the SiS abundance is however much more clear for the M-type stars, when stars with a much wider range in mass loss rates are included as can be seen in Fig. 1.1 in chapter 1. One other reason that also can explain why no clear decrease with the mass loss rate is shown for the M-type stars is that the three stars', WX Psc, IRC-10529 and R Cas, results are worsen the chance to find a correlation between the mass loss rate and the SiS abundance. These three stars will be further discussed in the next section.

6.4 Special objects

All the three M-type stars, RCas, IRC-10529 and WX Psc are stars that have mass loss rates that are more difficult than usual to estimate. This means that their mass loss rates are varying with time. A much more accurate estimate of these stars mass loss rates would be done if the models could take account for mass loss rate's variation with time, for further discussion see Schöier et al. (2007), in prep.

Both R Cas and IRC-10529 have a much lower abundance of SiS than expected for their mass loss rates, if a correlation should be found between the mass loss rates and the SiS abundances for the M-type stars. According to very recent estimations by Schöier et al. (2007), in prep. has R Cas a mass loss rate of $4.0 \cdot 10^{-6}$ closer to the star which would be more appropriate for the SiS modelling instead of the $1.1 \cdot 10^{-6}$ that is used in the model now. The reason for this is that the observed SiS line emission is coming from the inner regions of the CSE. To see how this new mass loss rate would affect the results was the star remodelled with the new mass loss rate. This gave a new abundance of $3.5 \cdot 10^{-8}$ instead of $1.5 \cdot 10^{-7}$, in this remodelling was not the photodissociation

radius r_e changed. If this had been done had probably the abundance decreased even more. A new lower abundance for R Cas would improve the r-value for the M-type stars but still not as much so that a strong correlation could be found between the mass loss rates and the amount of SiS molecules.

The star WX Psc is also special because of its much higher abundance than expected for a M-type star. This star is well known to be acting in a more unusual way, which for example makes it hard to properly estimating its mass loss rate. A new r-value was calculated with the removal of WX Psc and R Cas from the sample of M-type stars to see how this would affect the correlation value r. The result is interesting because without these two stars a correlation can be found for the M-type stars, the r value is then equal to -0.58 when the correlation is measured for the density measure $\dot{M}/v_e$ versus the SiS abundance.

6.5 High χ^2_{red}

The high χ^2_{red} for both types of stars fits obtained from the SiS modelling are interesting to look at. Especially when they are compared to the χ^2_{red} that are calculated for the fits between the SiO observations and their modelled lines, because they are much lower usually around 2-4, see Delgado et al. (2003) and Schöier et al. (2006). So the question is therefore why it is such a big difference in the agreement between the models and the observations for these two rather similar molecules. The same model and similar parameters have been used during the radiative transfer modelling so there is no explanation in how the results are derived from the model that might explain these differences. Two plausible explanations have been found. The first one is that SiS is more optically thin which in combination with the use of single dish telescopes and a steep abundance gradients might affect the observational results in a way that the model is not corrected for. The second explanation is that there is a temporal variation in the line intensities that is connected to the stars variable luminosity, this is also not included in the model which then will give modelled lines that differ from the observed lines. This will be further analysed and discussed in the upcoming sections.

6.5.1 The effects of a compact component of SiS

The model that has been used to describe the CSE envelope around the AGB star assumes that the SiS abundance f_0 is constant after the condensation radius r_i until it starts to decrease when the radius is getting closer to the photodissociation radius r_e. The same model is used when the SiO abundance i estimated. This model is used as an approximate way of describing how the SiO molecules are distributed in the CSE. According to recent interferometric observations by SiO in carbon and in M-type stars are the SiO molecules also gathered in a compact component in the inner parts of the CSE, see Schöier et al. (2006b). A question that is interesting to ask then is why such a good agreement is reached between the models and the observations of SiO, without having a compact component included in the models, see Gonzales Delgado et al. (2003) and Schöier et al. (2006). These articles show that the χ^2_{red} has rather low numbers for the most of the stars, which is stating a good agreement between the radiative transfer model and the observations.

The answer lies in the fact that the compact component will not affect the single dish observations of the SiO emission lines due to their high optical depths, ie. the line emission from the compact component will be absorbed by the outer parts of the CSE and never be detected in the observations. In addition to this will also the SiO emission be dominated by emission from the outer regions of the CSE because of the much higher A coefficient for the lower SiO rotational transitions, in the outer colder regions, than for the higher SiO rotational transitions in the inner warmer part of the CSE. So the emission from a compact component would even be hard to detect if the line emission would have been optically thin. This concludes that a model without a compact component can be used to describe the CSE morphology with good agreement with the observations.

A compact component will however affect the observations of the optical thin SiS line emission, because then the emission from the compact component will pass through the CSE and reach the telescope. This means that the single dish observations will both receive SiS line emission from the inner compact component and the outer cooler regions in the CSE. If this is not taken account of in the model it will cause disagreements between the model and the observations and therefore give high χ^2_{red}.

From the above discussion can the conclusion be drawn that an inclusion of a compact component in the model might improve the χ^2_{red}. This was therefore done, see section 5.1, and the results showed that 2 of 8 stars fits were improved. The common thing for both these stars were that they were both M-type stars and that they had low abundances of SiS compared to the other stars in the test. This was agreeing well with the results from the investigation where the I_{comp} / I ratio was calculated for an example star where just the mass loss rate and SiS abundance were changed. Because the results showed that the higher lines and stars with lower SiS abundances were more sensitive to changes in the condensation radius r_c than the lower lines and stars with higher SiS abundances. According to these results all the M-type stars would be more sensitive to a compact component than the carbon stars because of their lower SiS abundances. So the carbon stars and the M-type star WX Psc should not be affected so much because of their higher SiS abundances. The other two M-types stars' χ^2_{red}, with low SiS abundances, were however not improved by the inclusion of a compact component as would have been though from the investigation. The reason for this could be that they did not have any compact component in them or that other things like varying line strengths are affecting the intensities of the observed lines (see section 6.5.2.

The same investigation also showed that the SiO I_{comp} / I ratio was not sensitive for a compact component as the SiS I_{comp} / I ratio was in the, SiS abundance and mass loss rate, region were this diploma thesis sample was placed. This is agreeing well with the earlier discussion about how these molecules single dish data would be affected by a compact component in the model.

Interferometric observation of SiS that have been done can be seen in the articles Bieging and Tafalla, (1993) and Lindqvist et al. (2000). They are there presenting one SiS map each. In Bieging and Tafalla, (1993) is CW Leo studied, see Fig. 6.6(a) and RW LMi is observed in Lindqvist et al. (2000), see Fig. 6.6(b). The major conclusion that can be taken from these both diagrams is that most SiS molecules are formed in the photospheres of the stars because the line intensity is highest closest to the star and then falls off. In Lindqvist

et al. (2000) is the brightness temperature just decreasing in a similar way as the synthesized clean beam which will not give so much information about how the SiS molecules are distributed in the CSEs of the AGB stars. It is instead more interesting to study the SiS line emission intensity in Fig. 6.6(a) which is clearly resolved. A broader halo of emission from 6" and outwards can be seen in this figure. These figures are not giving any clear indication of an existing compact component in the stars but modelling of these data and future similar interferometric observations can investigate that.

6.5.2 Variation of lines with the luminosity of the star

The high χ^2_{red} might also be explained by the low intensity in the J = 6-5 line for some of the stars. According to the model emission from the J = 6-5 line should be stronger than the J = 5-4 line (for the same telescope), not equal or weaker than what is observed in many of the stars. This will cause a bad fit between the modelled and observed lines. The results from table 5.2 is also supporting this. Even when the stars luminosity is set to zero and the dust is taken away is the intensities for the J = 6-5 line still much stronger than the 5-4 line, which is not agreeing with the observations.

A natural explanation would be time variation in the line intensities. This is very interesting to have in mind when reading about the results that have been published by Carlström et al. (1990). They have in this article been observing a time variation in the line intensities and line profiles of the J = 6-5 and J = 5-4 lines that is correlated with the IR-flux in the K-band for the carbon star CW Leo, see Fig. 6.7. It can there be seen that the $I(\mathrm{SiS})/I(\mathrm{HC_3N})$ ratio for J = 5-4 is decreasing and increasing for J = 6-5 when the K magnitude is decreasing. This means that both the emission lines are varying with the stars variability period and that they do it in opposite ways. This might explain the stronger J = 6-5 lines. They were maybe observed at their maximum while the J = 5-4 lines were observed at their minimum. These variations are so large that they would be able to explain the high χ^2_{red}-values, because they were not included in the model. They will however not affect the results so much so that the difference between the M-type stars and carbon stars and the variation with the mass loss rate could be explained. According to estimates will the line intensity variations not affect the SiS abundances with more than 50 %. This phenomena has so far just been studied in one stars lower rotational transitions so it is still to early know how much similar processes might influence the results. Further observations have to be made on additional stars and on more and higher rotational transitions to take any certain conclusions. One hypothesis that is presented in Cherchneff's article to explain the time variations in the line intensities is that is occurring line overlapping from another molecule than SiS that is affecting the SiS emission lines.

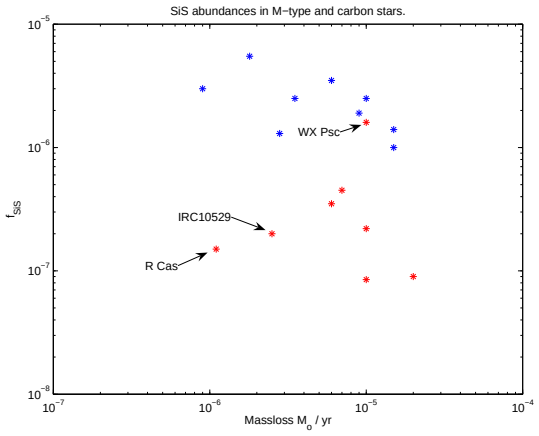

(a) The estimated SiS abundances from modelling.

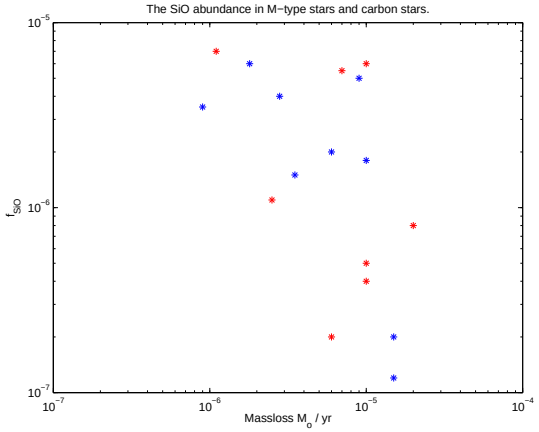

(b) The estimated SiO abundances from Gonzales Delgado et al.(2003) and Schöier et al. (2006).

Figure 6.2: A comparison between the estimated SiS and SiO abundances for the same sample of stars.

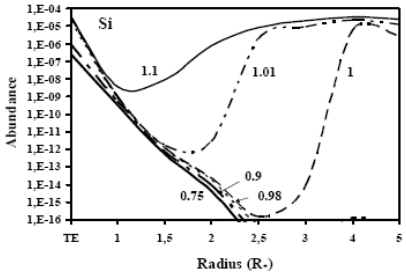

(a) The S TE abundance versus C/=O ratio (curve labels) and stellar radius.

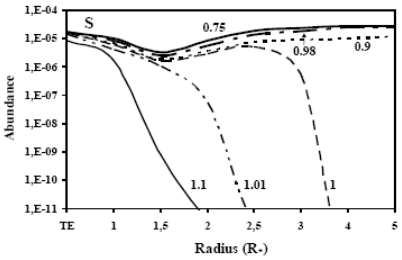

(b) The Si TE abundance versus C/=O ratio (curve labels) and stellar radius.

Figure 6.3: The estimated Si and S abundances from the chemical models in Cherchneff et al. (2006)

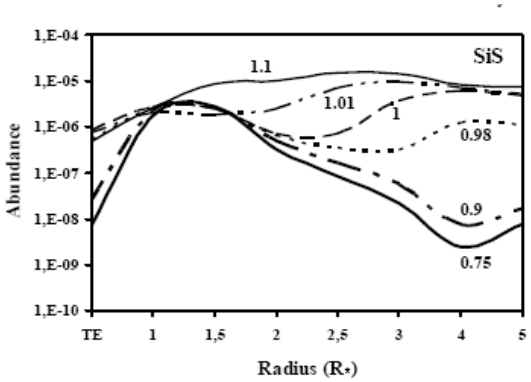

Figure 6.4: The SiS TE abundance versus C/=O ratio (curve labels) and stellar radius, Cherchneff et al.(2006)

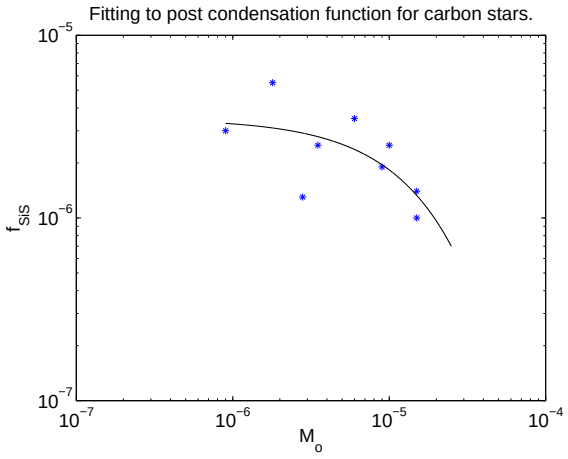

(a) Carbon stars data.

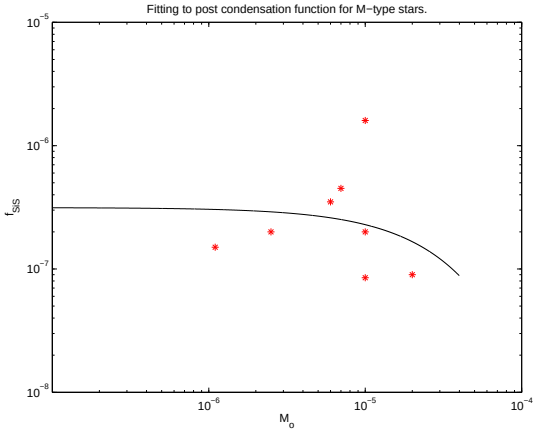

(b) M-type stars data.

Figure 6.5: A post condensation function that is fitted to the carbon stars and m-type stars data.

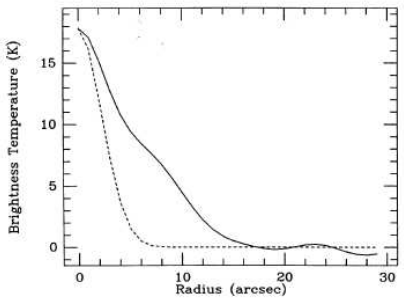

(a) Brightness temperature of SiS emission as a function of radial distance for the star CW Leo. The dashed curve shows the radial profile of the synthesized clean beam. Taken from Bieging and Tafalla, (1993)

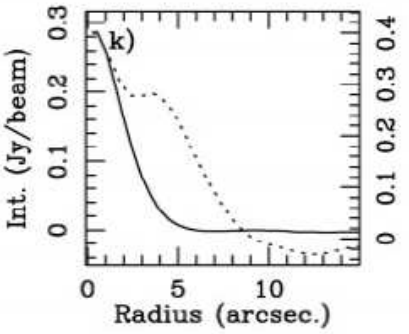

(b) The radial brightness profile of SiS (J = 5-4) (solid line) and HC_3N (J = 10-9) (dashed line) emission of the star RW LMi. Taken from Lindqvist et al. (2000)

Figure 6.6: Results from interferometric observations of SiS emission of the two stars CW Leo and RW LMi. These results are taken from Bieging and Tafalla, (1993) and Lindqvist et al. (2000).

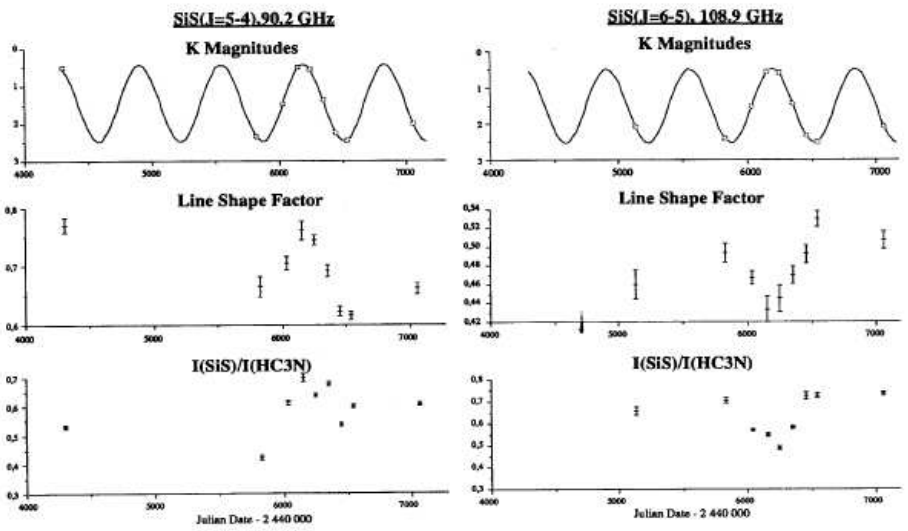

Figure 6.7: The correlation between the IR-intensity, line shape and relative intensity for the rotational transitions J = 6-5 and J = 5-4, Carlström et al.(1990)

Chapter 7

Conclusions

The two major goals with this diploma thesis have been to estimate accurate circumstellar SiS abundances in AGB stars and too look for possible correlations with stellar parameters such as mass loss rate and photospheric C/O-ratio. 34 AGB stars have been observed by three radio telescopes; JCMT, APEX and the Onsala 20 m telescope. SiS was detected in 17 of them, in 9 carbon stars and 8 M-type stars. A detailed Monte Carlo radiative transfer code was used to derive reliable SiS abundances from the observations. The results show that the SiS abundances is about a factor of ten higher in carbon stars than in M-type stars. The median value of the SiS fractional abundance for the carbon stars was $2.5 \cdot 10^{-6}$ and for the M-type stars $2.1 \cdot 10^{-7}$, the uncertainty for an individual object is estimated to be at most a factor of 3-5 depending on the mass loss rate. The SiS abundance in carbon stars is agreeing rather well with predictions from recent chemical models. However, there are discrepancies for the SiS abundance in M-type stars where theory predicts significantly lower values than what is observed.

A rather strong correlation was found for the carbon stars, between the SiS abundance and the mass loss rate. These results, like those of SiO in a similar study, are showing a tendency for the molecules to condense onto dust grains at higher mass loss rates in the outer parts in the AGB star's CSEs. This means that these molecules are incorporated to some degree into dust grains and may be protected from dissociation as they leave the stars. This opens up the possibility that they can be distributed into the interstellar medium. A similar correlation is found for the M-type stars if sources with known peculiarities in their CSE are neglected. The inclusion of a broader sample of objects might improve the correlation for both the carbon and M-type stars.

Additional interferometric observations is needed to learn more about the spatial distribution of the SiS molecules in the CSE envelope of the AGB stars. This would also give direct information about if there is a compact component of SiS in them or not. A lot of challenging work with developing and refining the chemical models is left to be done in the future in order to make them more reliable for comparison with the observations. Also both the radiative transfer and chemical models need to be adjusted and changed so that they can include inhomogeneities like clumps and compact components in their description of the CSEs. Further studies of how the SiS lines from AGB stars are varying with their IR-intensity would also be very interesting to do.

Acknowledgements

I first of all want to thank my supervisor Fredrik Schöier for all his work with this diploma thesis and especially for his encouragement, support, patience and many advises. I am so very grateful for the fact that you never give up on me, this have made me to work so much better than I ever thought that I could do. I am also very grateful to Hans Olofsson for his comments and feedback and to all the nice people at the Astronomy department that have made my stay there to such a great time. I finally want to thank my very close and dear friend Sara Rydbeck for always making me believe in myself.

Bibliography

[] Bernes, C., 1979,A&A,73, 67

[] Bieging, J. H., Tafalla, M., 1993, AJ, 105, 576

[] Bujarrabal, V., Fuente, A., Omont, A., 1994, A&A, 285, 247

[] Carlstrom, U., Olofsson, H., Johansson, L. E. B., Nguyen-Q-Rieu, Sahai, R., 1990, fmpn, coll, 170C

[] Cherchneff, I., 2006, A&A, 456, 1001

[] Christensen-Dalsgaard, J., 2003, *Stellar Structure and Evolution*, Institutionen for Fysik og Astronomi, Aarhus Universitet

[] Duari, D, Cherchneff, I, Willacy, K., 1998, IAUS, , 191P, 232

[] Emerson, D., *Interpreting astronomical spectra*, 1997, John Wiley & Sons Ltd

[] Groenewegen, M. A. T., Whitelock, P. A., 1996, MNRAS, 281, 1347

[] González Delgado, D., Olofsson, H., Kerschbaum, F., SchÃűier, F. L., Lindqvist, M., Groenewegen, M. A. T., 2003, A &A, 411, 123

[] Habing, H. J., Olofsson, H., *Asymptotic giant branch stars*, 2004, Springer

[] Kitchin, C. R., *Astrophysical Techniques*, 2002, Institute of Physics Publishing

[] Kholopov P.N et al. 1985, General Catalogue of Variable Stars, 4:th ed., Moscow Publishing House

[] Lambert, D. L., Gustafsson, B, Eriksson, K., Hinkle, K. H., 1986, ApJ, 62, 373

[] Lindqvist, M., Schöier, F. L., Lucas, R., Olofsson, H., 2000, A&A 361, 1036

[] Olofsson, H., Lindqvist, M., Nyman, L.-A., Winnberg, A., 1998, A&A, 329, 1059

[] Sackmann, I.-J., Boothroyd, A. I., Kraemer, K. E., 1993, ApJ, 418, 457

[] Schöier, F. L., 2000, PhD Thesis, Stockholm Observatory

[] Schöier, F. L., Olofsson, 2001, A&A, 368, 969

[] Schöier, F. L., Ryde, N., Olofsson, H., 2002, A&A, 391, 577

[] Schöier, F. L., van der Tak, F. F. S., van Dishoeck, E. F., Black, J. H., 2005, A&A, 432, 369

[] Schöier, F. L., Olofsson, H., Lundgren, A., 2006, A&A, 454, 247

[] Schöier, F. L., Fong, D., Olofsson, H., Zhang, Q., Patel, N., 2006b, ApJ, 649, 965

[] Schöier F. L., 2007, *Why Galaxies Care About AGB Stars*, conf., Vienna

[] Schöier et al. in prep. 2007

[] van Zadelhoff, G.-J., Dullemond, C. P., van der Tak, F. F. S., Yates, J. A., Doty, S. D., Ossenkopf, V., Hogerheijde, M. R., Juvela, M., Wiesemeyer, H., Schöier, F. L., 2002, A&A, 395, 373

[] Whitelock, P., Menzies, J., Feast, M., Marang, F., Carter, B., Roberts, G., Catchpole, R., Chapman, J., 1994, MNRAS, 267, 711

[] Woods, P. M., Schöier, F. L., Nyman, L.-Å., Olofsson, H., 2003, A&A, 402, 617

Appendix A

Reduced spectra

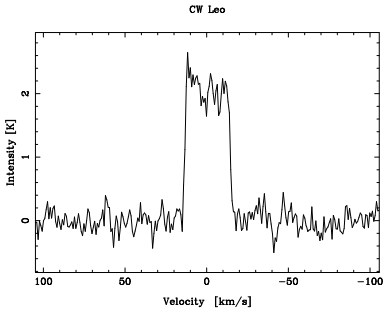

(a) CWLeo, SiS(5-4), 0.8 km/s

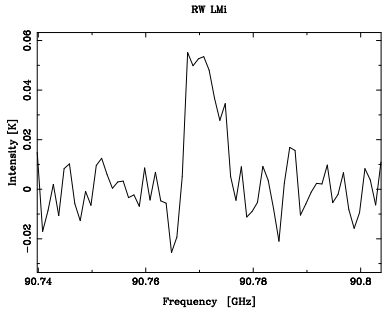

(b) RWLMi, SiS(5-4), 3.3 km/s

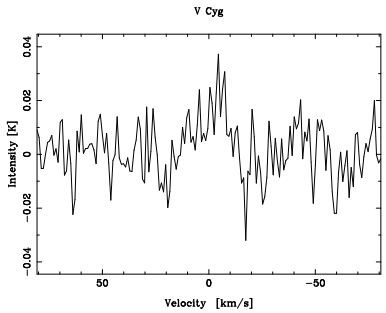

(c) VCyg, SiS(5-4), 1.0 km/s

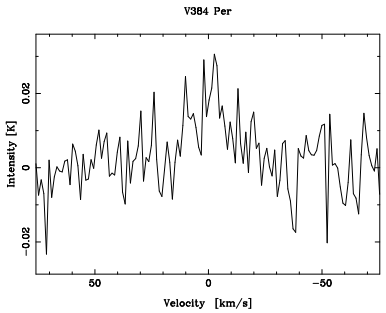

(d) V384Per, SiS(5-4), 1.2 km/s

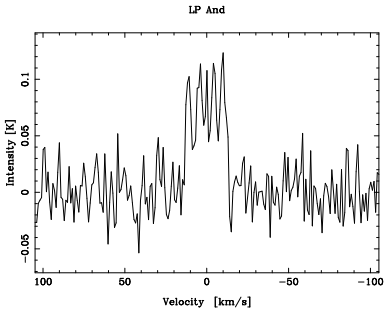

(e) LPAnd, SiS(5-4), 1.0 km/s

Figure A.1: OSO, carbon stars

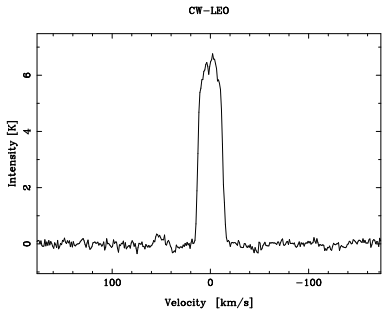

(a) CWLeo, SiS(20-19), 1.0 km/s

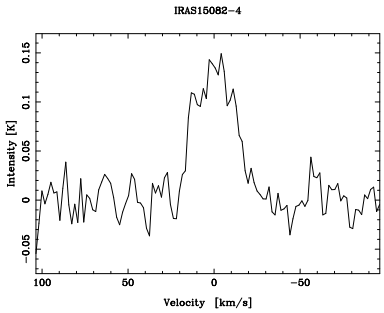

(b) IRAS15082, SiS(19-18), 1.7 km/s

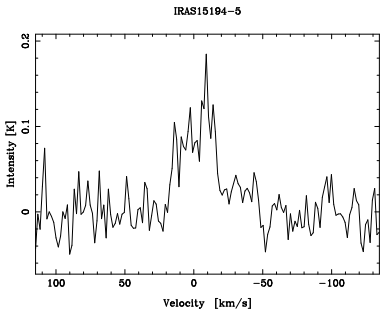

(c) IRAS15195, SiS(20-19), 1.7 km/s

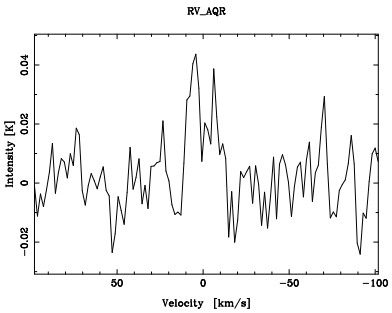

(d) RVAqr, SiS(19-18), 1.7 km/s

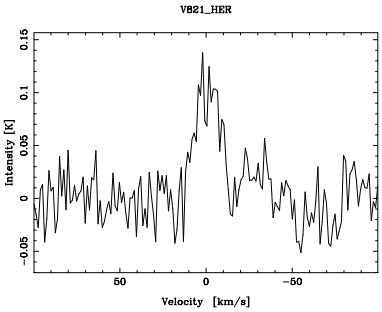

(e) V821Her,SiS(20-19), 1.2 km/s

Figure A.2: APEX, carbon stars

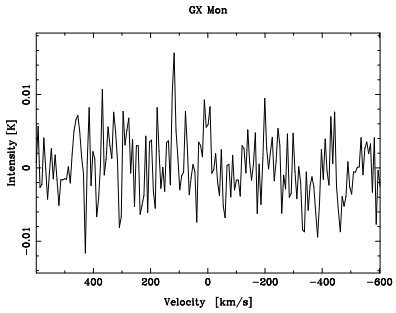

(a) GXMon, SiS(5-4), 6.6 km/s

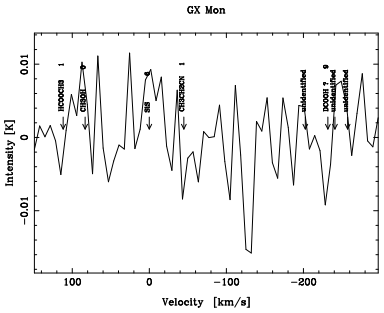

(b) GXMon, SiS(6-5), 6.9 km/s

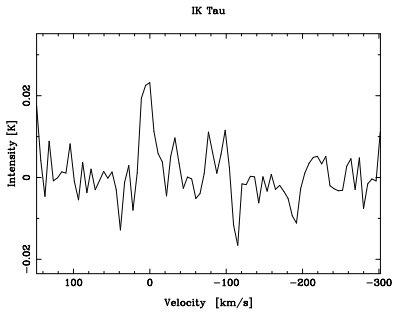

(c) IKTau ,SiS(6-5), 5.5 km/s

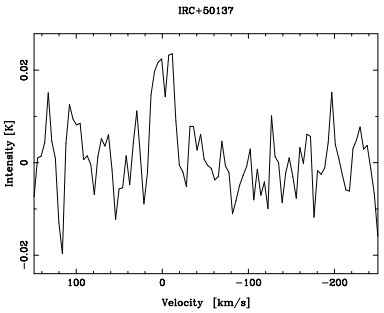

(d) IRC50137, SiS(6-5), 4.1 km/s

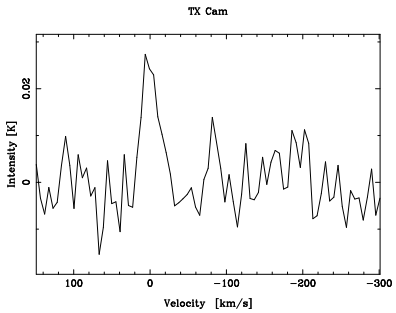

(e) TXCam, SiS(6-5), 5.5 km/s

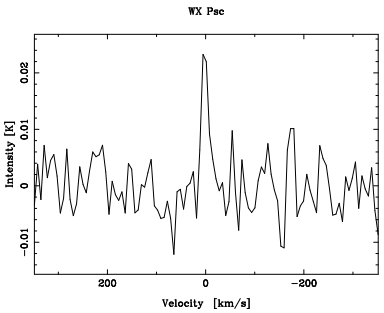

(f) WXPsc, SiS(5-4), 6.6 km/s

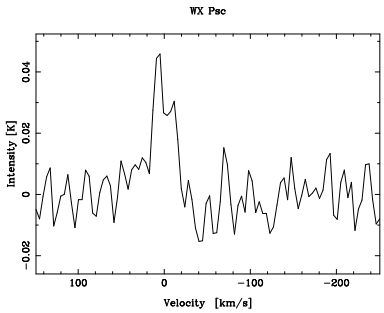

(g) WXPsc, SiS(6-5), 4.1 km/s

Figure A.3: OSO, M-type stars

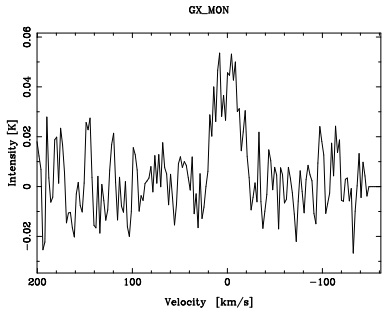

(a) GXMon, SiS(12-11), 2.1 km/s

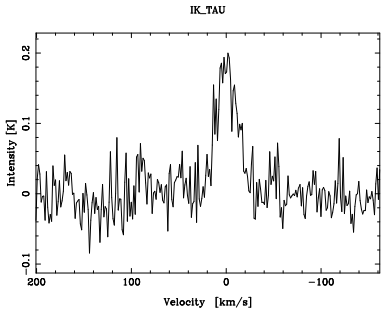

(b) IKTau, SiS(12-11), 1.4 km/s

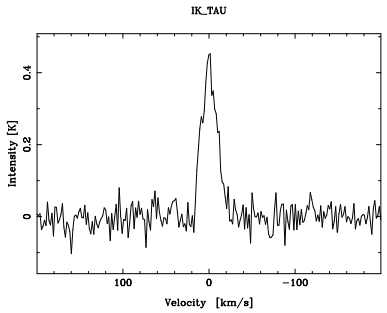

(c) IkTau, SiS(19-18), 1.7 km/s

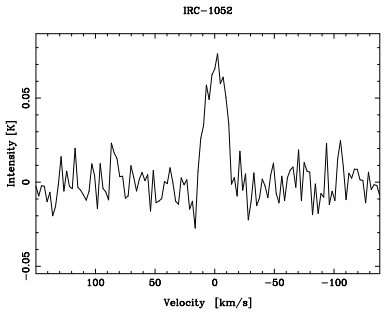

(d) IRC10529, SiS(12-11), 2.3 km/s

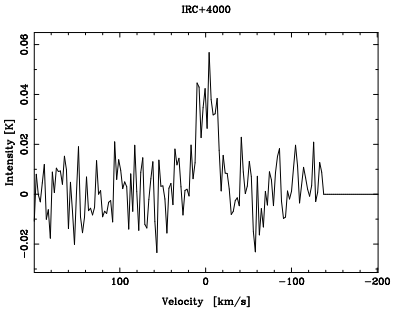

(e) IRC40004, SiS(12-11), 2.3 km/s

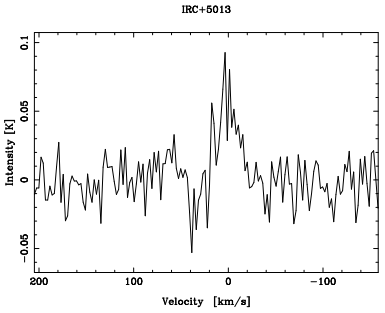

(f) IRC50137, SiS(12-11), 2.3 km/s

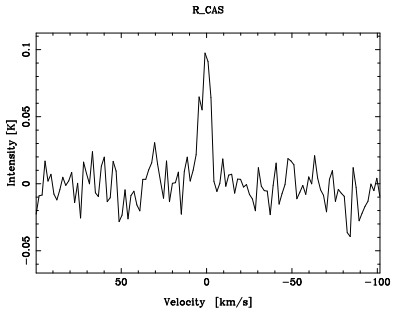

(g) RCas, SiS(19-18), 1.7 km/s

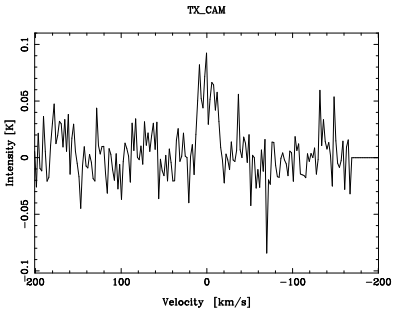

(h) TXCam, SiS(12-11), 2.1 km/s

Figure A.4: JCMT, M-type stars

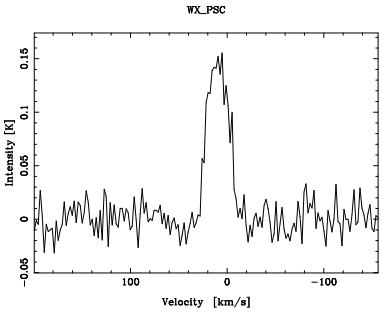

Figure A.5: continuation of JCMT, M-type stars: WXPsc, SiS(12-11), 2.1 km/s

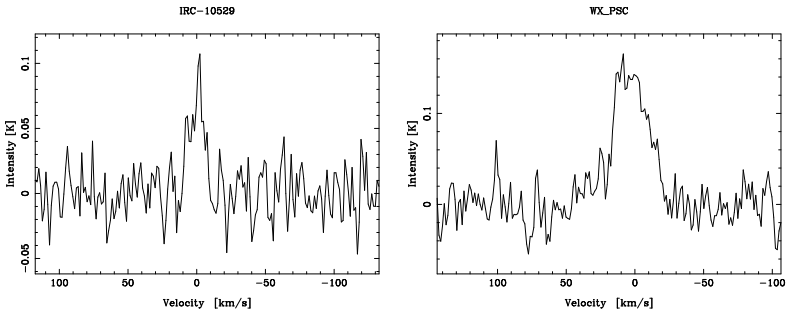

(a) IRC10529, SiS(19-18), 1.3 km/s

(b) WXPsc,SiS(19-18), 1.3 km/s

Figure A.6: APEX, M-type stars

Appendix B

The proposal to the APEX telescope